MAX-PLANCK-GESELLSCHAFT

Inorganic crystallization at the interface in miniemulsion systems

Master Thesis

by

Hasan Samet Varol

Ulm University, Advanced Materials

Max Planck Institute for Polymer Research

Mainz, 2012

First Referee: Prof. Dr. Katharina Landfester
Second Referee: Dr. Ulrich Ziener
Supervisors: Prof. Dr. Katharina Landfester, Dr. Ulrich Ziener, Dr. Rafael Muñoz-Espí

Application date: 18 April 2011
Completion date: 18 January 2012

I confirm that the presented master thesis is an original work, completed independently without inadmissible help.

Ulm, 18 January 2012

Hasan Samet Varol

I would like to dedicate this thesis

to my beloved sister

Table of contents

Chapter 1

Introduction

Current developments in nanoparticle formation are stimulating novel applications in many research fields of academia and industry. Especially, the hierarchical assembly offers great opportunities for the spontaneous formation of structures.[1] The relationship between functional and geometrical properties plays an important role in many applications of micro- and nanostructured materials.[2] For instance, catalytic, sensing, and photovoltaic activities have a strong dependence on the effective surface area; thus, porous and hollow materials come into prominence for these applications. Additionally, controlled release of molecules, gas adsorption, and structural building units for ultrasonic imaging have been reported,[3] increasing the importance of hollow particles.

Both organic-including polymeric-and inorganic species can form hollow spheres. In contrast to organic counterparts, inorganic materials may provide better magnetic, electrical, thermal, optical, electrochemical, mechanical, and catalytic properties.[4-9]. Compared with solid particles, inorganic hollow spheres have a lower density, high surface-to-volume ratio, and low thermal expansion coefficients, which can be advantageous in applications like biomedicine,[10] waste water treatment,[11] lithium-ion batteries,[10] catalysis, and sensing.[12]

Controlled synthesis of hollow materials can be classified in two main groups: (i) *templated methods*, which include hard template and soft template routes, and (ii) *non-templated* (or template-free) *methods*. The *hard-template route* is the most common approach to form nanosized capsule.[13-15] However, the removal of the hard (solid) template is a complicated and energy consuming process, and it can generate structural degradation of the nanoparticles. The *soft-template route* is an alternative way to obtain hollow particles by using surface-active agents in heterophase systems. Emulsions (mini- or microemulsions) are very convenient systems to produce hollow structures in presence of the amphiphilic surfactants, which have the ability to self-assemble into organized structures.

Recent efforts in chemistry and physics have shown us the importance of iron oxides by revealing their wide range of application fields, such as biotechnology, medicine, electromagnetic devices, and magnetoelectronics.[16-21] Today, nanoscience researchers are more interested in the dependence of properties such as superparamagnetism or catalytic activity on

morphology and structure. Srivastova et al. reported a method to prepare hollow Fe_2O_3 particles by sonochemical synthesis and they indicated that these Fe_2O_3 capsules exhibit excellent catalytic properties in the oxidation reaction of cyclohexane.[12] Li and coworkers have also synthesized Fe_2O_3 hollow particles by using a non-templated route involving a hydrothermal process.[22] They claimed that the photocatalytic properties of the Fe_2O_3 capsules are superior than other Fe_2O_3 particles. Much research in biomedicine has been focused on the integration of superparamagnetic and hollow structure of iron oxides for high-capacity drug loading and targeted drug delivery. In this sense, Cao et al. reported a precursor-templated conversion method to synthesize highly magnetic and biocompatible hollow spheres, assembled to Fe_3O_4 and γ–Fe_2O_4 nanosheets.[23]

The development of a simple and effective synthetic method to obtain superparamagnetic nanocapsules is still an unresolved task. Hence, soft-template pathways have priority among other methods to obtain iron oxide nanocapsules; unfortunately, these methods have not been well established yet. Chen and coworkers have reported a solution-phase approach to synthesize Fe_3O_4 capsules in ethylene glycol solution in absence of any surfactant and template.[24] However, the magnetization of the capsules did not show a superparamagnetic behavior and the process is still time and energy consuming (e.g., thermal treatment in autoclave at 200 °C for 12 h).

Cerium(IV) oxide (or ceria) is one of the other intriguing metal oxides in nanomaterials science due to its oxygen storage capacity, oxygen deficiency, and electronic conductivity.[25] These benefits are useful in fields such as heterogeneous catalysis, chemical sensors, artificial cells, chemical reactors, and drug delivery carriers.[26-27] Morphological and microstructural differences have a great influence on the performance of ceria. Among the different possible morphologies, including nanoparticles,[28-29] nanowires,[30] and nanocubes,[31-32] ceria hollow nanospheres are especially relevant due to the large specific surface area, stability, low density, good surface permeability, and distinct optical properties.[33]

In this work, exemplified for the cases of iron and cerium oxides, we study the precipitation of transition metal oxides at the droplet interface in both water-in-oil and oil-in-water miniemulsion systems. We analyze thereby the effects of the synthetic parameters, including the type of surfactant, the added base and the precursor used. To the best of our knowledge, this thesis reports for the first time a facile soft-template method to produce hollow spheres of ceria and various iron-oxides in the nanometric scale.

Chapter 2

Background of the work

2.1 Inorganic crystallization on heterophase systems

This section provides the theoretical background of the thesis by explaining the basics of crystallization in heterophase systems in terms of phase separation and the subsequent crystallization from supersaturated solutions. These two phenomena will be helpful for the understanding of the following theoretical concepts.

In simple terms, phase separation is the process that separates a homogeneous liquid into two immiscible liquid phases as it enters an immiscibility dome.[34] Correspondingly, this unmixing process leads to two possible mechanisms: (a) the nucleation and growth, and (b) the spinodal decomposition. Chan and Hillert[35-36] explained the difference of these two mechanisms in terms of free energy change due to small fluctuations in the composition of the liquid.

To be able to understand the free energy change, we need to explain more about the influence of thermodynamic factors on the immiscibility of two liquids. If a particular composition gives a mixture of two liquids rather than a single phase liquid, it means that this assemblage has a lower free energy than the single liquid phase with the same composition. It is easier to explain the concept of free energy dependence on the immiscibility formation by writing the free energy rule in terms of enthalpy (ΔH), entropy (ΔS), and temperature (T):

$$\Delta G = \Delta H - T\Delta S \tag{2.1}$$

According to the equation of free energy, two liquids are miscible if $\Delta G < 0$ and immiscible in $\Delta G > 0$ conditions due to the changes of the thermodynamic factors in the equation.

The two mechanisms of phase separation are represented in Figure 1. The free energy change in variable compositions is presented for two different temperatures, T_1 and T_2. Liquid immiscibility only occurs at T_2. Due to the single phase of the liquid for all compositions, at T_1 no immiscibility is observed. Additionally, a decrease in free energy occurs at T_1 for mixing of the two liquids at any ratio.

At temperature T_2, immiscibility occurs at any composition between *a* and *b* due to the free energy curve, with minima at both *a* and *b* for two stable liquids. When the effect of small

compositional fluctuations in a single phase liquid at T_2 is investigated, the behavior of compositions between *c* and *d* is different from the other compositions shown in the free energy curve. The mechanism of *nucleation and growth* occurs in any composition between *a* and *c* or *b* and *d*, and it results from a separation of the liquid into two phases due to a net increase in free energy. However, all the compositions between *c* and *d* culminate as a decrease in free energy. Correspondingly, a spontaneous and unstable separation into two liquids occurs, the so-called *spinodal decomposition*.

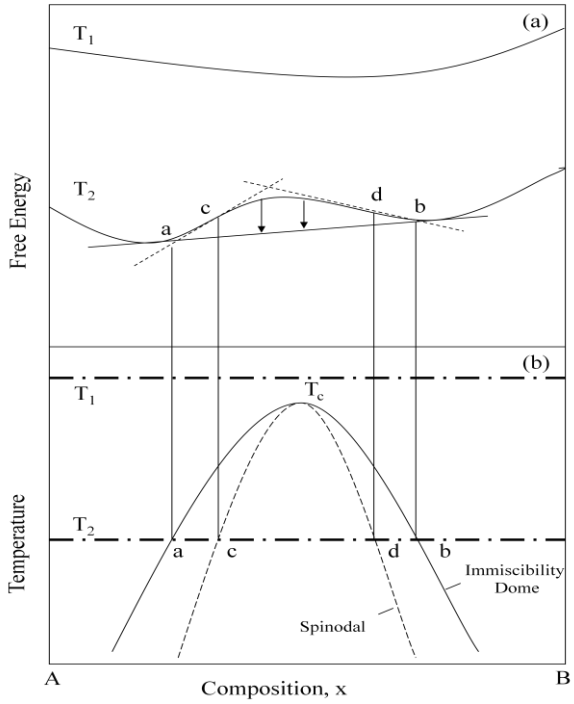

Figure 1. Free energy curve representing the free energy changes for two different temperatures, T_1 and T_2 (adapted from ref. [34]).

Crystal formation from a supersaturated solution can be explained by nucleation, crystal growth, and ripening. *Nucleation* is the initial step of crystallization by the formation of *nuclei*, which act as a center from which spontaneous growth takes place. Nuclei can be generated by *primary nucleation* in absence of any crystalline matter in the supersaturated system. There are two types of primary nucleation: *homogenous nucleation*, which occurs in an identical phase, and *heterogeneous nucleation*, which is induced at centers of defects and higher local free energy sites.[34] Furthermore, *secondary nucleation* can occur when nuclei are generated in existence of crystals in the system. Subsequently, *crystal growth* takes place by ordered deposition of material around the formed nuclei. Finally, the *ripening* step occurs by dissolving and transferring small particles to the larger ones in solution. The crystal formation in steps is represented in Scheme 1.

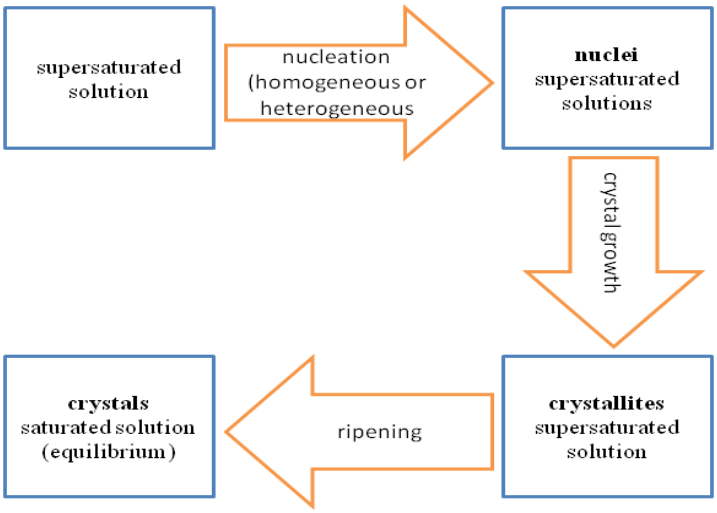

Scheme 1. Steps of crystal formation (adapted from ref. [37]).

2.2 Confined crystallization

Using confined systems provides the opportunity to direct the particle formation of inorganic materials due to, for instance, the templating effect of an organic matrix. Recent studies show that micelles[38-39], emulsions[40-41] or lamellar phases[42-43] can be efficiently used as templating matrices. Furthermore, the inorganics synthesized in any of these confined systems may also provide new improvements to the organic entities, such as biocompatibility.[44] In our study, we have aimed to reach interfacial crystallization of inorganics in emulsion systems. One advantage of emulsion systems is the ability to improve the physical properties of the liquid droplets due to the high surface-to-volume ratios. The physical properties of the emulsions can be also modified in parallel to the physical properties of the droplets.[45] Crystallization within confined droplets in emulsion systems provides a simple method to synthesize nanosized particles, which have an increasing importance in both biological and materials science research.[46]

2.2.1 Miniemulsion systems

Briefly explained, an emulsion is a system containing liquid droplets (disperse phase) in another immiscible liquid (continuous phase). According to the chemistry of the disperse and continuous phase, emulsion systems are divided in oil-in-water (direct) and water-in-oil (inverse) emulsions. Landfester, one of the pioneers of miniemulsion systems, has demonstrated the versatility of miniemulsions among other emulsion systems (macro- and microemulsions).

Miniemulsions are specially formulated heterophase systems containing critically stabilized nanodroplets with size between 50 and 500 nm.[47]

A basic schematic representation of a miniemulsion process is shown in Figure 2. In the first step, a system containing a disperse phase in presence of an osmotic pressure agent and the continuous phase with a surfactant undergoes a shearing process, and small stable droplets are formed. In the second step, a reaction takes place inside these droplets without changing their identity.

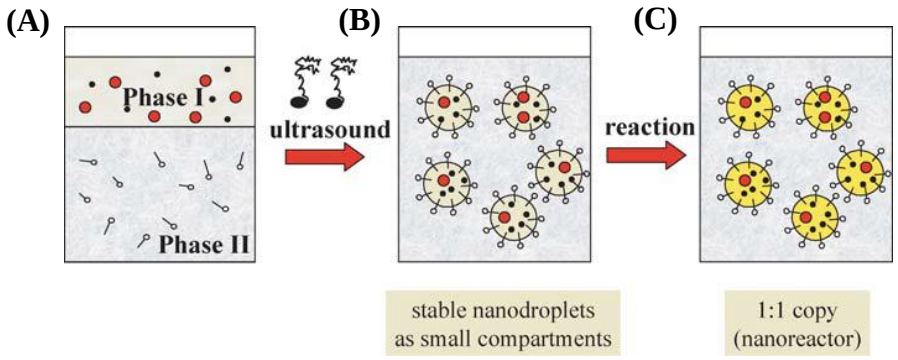

Figure 2. Scheme of the miniemulsion process.[47]

The conduction of reactions—such as polymerization or crystallization reactions—within miniemulsion droplets offers a wide range of possibilities for the formation of structured nanoparticles.[47] Crystallization can be also driven to the droplet interface in miniemulsion systems to achieve inorganic hollow particles,[48-50] which is the aim of our work.

Stability of miniemulsions

Two main processes, schematically depicted in Figure 3, can lead to the destabilization of emulsions: coalescence and Ostwald ripening. *Coalescence* occurs by collision of two droplets due to van der Waals attractive forces. *Ostwald ripening* process takes place by mass diffusion from a smaller droplet to a bigger one. The mass diffusion is driven by the different Laplace pressure and chemical potentials of these droplets. The Laplace pressure, Δp, is expressed as:

$$\Delta p = \gamma \frac{2}{r} \tag{2.2}$$

where γ is the oil/water interfacial tension and r is the droplet radius.

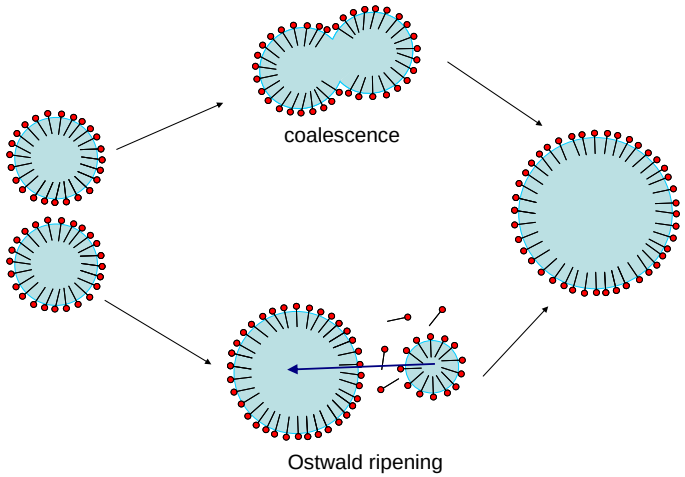

Figure 3. Schematic representation of Ostwald ripening and coalescence of particles.[37]

The surface tension has a tendency to compress the droplet and increase the internal pressure. Different chemical potentials can cause osmotic pressure (Π), balancing the Laplace pressure. The osmotic pressure is given by the following equation proposed by van't Hoff:

$$\Pi = nRT/V \tag{2.3}$$

where R is the gas constant, T is the temperature and n/V gives the molar concentration.

A stable miniemulsion can only be achieved by avoiding coalescence and Ostwald ripening. The oil/water interfacial tension can be decreased by surfactant addition, which avoids coalescence. We can also prevent Ostwald ripening by adding a *hydrophobic agent* (*costabilizer* or *cosurfactant*), such as hexadecane or other long-chain alkanes.

In order to avoid coalescence and, therefore, to obtain better stability of a miniemulsion system the following three strategies can be used:

I. *Electrostatic stabilization*: repulsion between the same surface charge particles will tend to avoid aggregation and cause a stabilization of the system (e.g., the use of charged surfactants leads to electrostatic stabilization).
II. *Steric stabilization* is achieved by a hydrophobic layer onto the particle surface.
III. *Electrosteric stabilization* occurs under both steric and electrostatic stabilization conditions together.

2.3 Inorganic capsules and crystallization at the interface

The ability to improve flow performance and high surface areas of porous capsules has attracted the attention of many researchers in recent years. Void interior of capsules can be used as a storage space to encapsulate various substrates that can be released afterwards.[51-54]

Depending on the composition, hollow capsules can be divided in organic and inorganic ones. Organic (polymeric) hollow capsules can be prepared by coating the surface of a template particle, followed by the removal of these templates via etching.[53, 55-57] Moreover, emulsion polymerization, phase separation, cross linking of micelles and self-assembling can be used to synthesize organic capsules.[58-62] According to the tailored size, the sructure and the surface functional groups, the fabrication methods of inorganic capsules can be divided in templated (template-based) and non-templated (template-free) methods. Both fabrication methods allow us to achieve variable capsule morphologies (e.g., spherical,[63] spindle shape,[64] cubic[65]).

2.3.1 Templated and non-templated methods

Templated (template-based) routes: they are the most common approaches to fabricate hollow spheres, and can be divided in two categories: hard- and soft-template routes.

Hard-template routes involve the formation of a thin coating of the desired material (precursor) on the template to form a core–shell composition, followed by the removal of the template through calcination or selective etching with an appropriate solution. The inner diameter of a porous capsule is limited by the size of the template. Hard-template routes were effectively used to synthesize functional capsules, such as photocatalytic TiO_2,[13] magnetic Fe_3O_4,[15] and ultrathin SnO_2.[66] However, the requirements of using basic or acidic media or high temperature increase the cost and risk of large-scale manufacture.[67] Hyeon et al. proposed an alternative method whereby micro- and nanosized iron oxide rod or spheres are generated first; while growing the capsules, they also act as a self-sacrificing template. By this technique they were able to produce hollow hematite or magnetite.[68]

In hard-template methods, the removal of the templates usually causes structural degradation. Thus, *soft template routes* are a good alternative for the preparation of inorganic hollow spheres. Organized systems like micelles, reverse micelles, vesicles *etc*., which are capable to self-assemble, are commonly used for soft-template routes. The *emulsion/phase separation*

procedure (Figure 4) is a very common method in soft templating. The systems prepared with this procedure include amphiphilic molecules (surfactants). These surfactants are first self-assembled in a solution (a), forming direct or reverse micelles. Subsequently, these systems are used as a template for hollow structures (b). Finally, these surfactants are removed with an appropriate solvent (c). Recently, Li and co-workers reported a method to synthesize SiO_2 nanocapsules with a tunable size by using this micellar aggregate templating route.[69] The phase separation route has also been utilized to synthesize functional inorganic capsules, such as high optical quality CuS,[70] multishelled Cu_2O,[71] biomimetic $CaCO_3$, [72] and superparamagnetic $CoFe_2O_4$. [73]

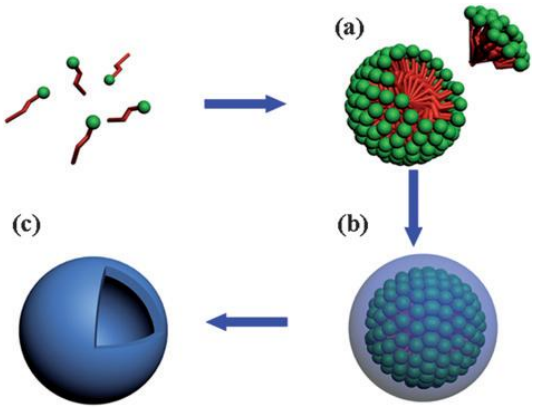

Figure 4. Schematic representation of typical emulsion/phase separation procedure for hollow inorganic capsules synthesis.[67]

Non-template (template-free) routes: The fabrication of inorganic capsules is mainly performed by soft- and hard-template methods; however, these routes are not very convenient for scaling up the practical applications because of their high cost and tedious synthetic steps.[67] Recently, a number of non-template approaches for hollow capsule synthesis were developed. In one-pot synthesis conditions, Ostwald ripening and oriented attachments are the most intriguing methods among the non-template ones. In a supersaturated solution, Ostwald ripening occurs due to attachment of the particles with different sizes to each other and, then, these large particles start to grow because of the energetic factors. The homogenization of the concentration gradient results in the elimination of the crystals with smaller size. Hollow spheres can be formed by controlling the size distribution and aggregation patterns of primary crystals.[67] Lu and coworkers reported a one-step non-templated synthesis of porous TiO_2 capsules by using this method, and the crucial point of their work is the observable morphological change of the capsules depending on the reaction time.[74]

Hollow capsules in a template-free approach can also be achieved by oriented attachment, which occurs due to the coalescence of faceted nanocrystals to avoid two high-energy facets.[75-76] As a brief description, the adjacent nanoparticles can be self-assembled in a common crystallographic orientation and they aggregate afterwards. If the aggregated blocks are convenient to generate a curvature geometry during their self-organizing process, the further architecture may result in a shell that is beneficial for the formation of hollow

structures.[67] Zeng et al. successfully demonstrated CuO spherical microspheres by using this strategy.[77]

2.4 Characterization methods

2.4.1 X-ray and electron diffraction

Identification of a crystalline material and unit cell dimensions can be conveniently analyzed by X-ray powder diffraction (XRD). The diffraction can be explained by resulting elastic scattering between the incoming beam and crystal atoms. A constructive interference is produced when incident rays interact with the sample. This constructive interference is obtained by Bragg's law:

$$n\lambda = 2d\sin\theta \tag{2.4}$$

where n is the order of diffraction, λ is the wavelength of incoming beam, d is the interplanar spacing, and θ is the diffraction angle. Bragg's law for first order diffraction (n=1) can be approximated when the wavelength of incoming beam electrons is much smaller than a typical X-ray.

Diffraction patterns obtained by conducting diffraction mode of a transmission electron microscopy (TEM) are achieved by focusing the projector lens on the back focal plane of the objective lens.

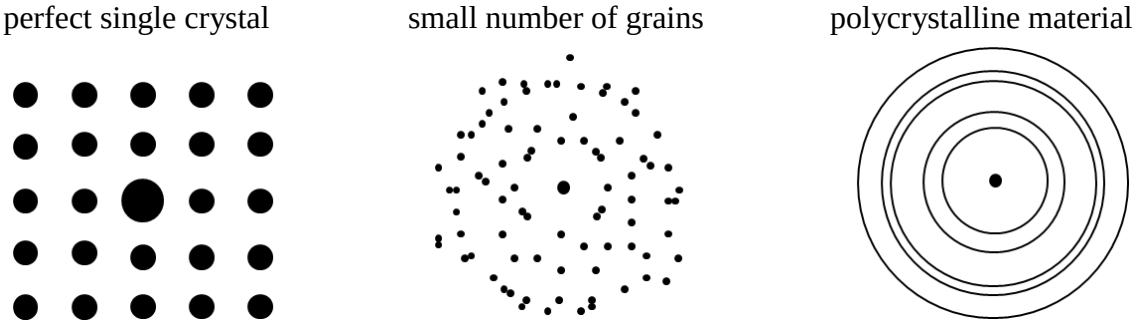

Figure 5. Typical electron diffraction patterns of crystalline materials

In our work, crystallinity of the inorganic samples was investigated by X-ray diffraction spectroscopy and electron diffraction mode of TEM.

2.4.2 Magnetic measurements

To be able to investigate the magnetic properties of the nanosized particles synthesized in this work, the magnetic measurement equipment should be sufficiently sensitive (performing measurements on media with a diameter of a few nm). Moreover, the analysis of the magnetization vector is more preferable for our view of investigation than the magnetization in the direction of the applied field because of the oblique anisotropy direction. These expectations can be covered by a vibrating sample magnetometer (VSM).

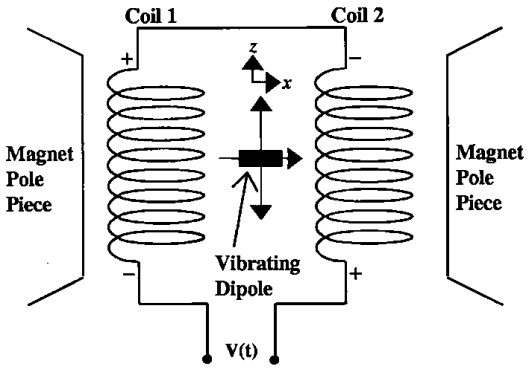

Figure 6. Setup and the working principle of VSM. [78]

Figure 6 represents a typical setup of a simple VSM. The magnetic powder sample is placed in a convenient capsule and vibrated in presence of a uniform and stable external field, which is generated by pick-up coils. The voltage, $V(t)$, is a measure of the magnetic moment of the sample and can be formulated as:

$$V(t) = C\frac{\mathrm{d}\Phi}{\mathrm{d}t} \qquad (2.5)$$

where Φ is the changing flux in the pick-up coils according to the movement of the sample.

2.4.3 X-ray photoelectron spectroscopy (XPS)

X-ray photoelectron spectroscopy (XPS) was performed to identify the elemental compositions of our samples. Moreover, the corresponding chemical state of the elements and the empirical formula can be determined by this technique. Basically, XPS analysis can exhibit the information in a gap close to the material surface (1 to 10 nm in depth) by irradiating the material with X-ray and analyzing the kinetic energy and number of electrons that escape the body.

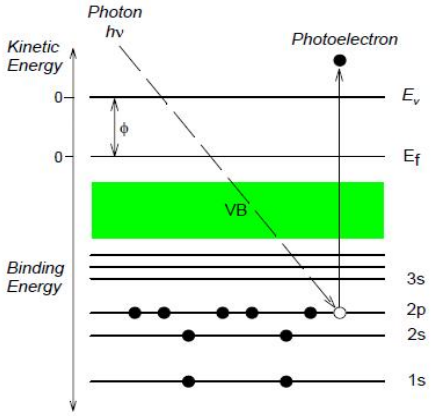

Figure 7. Schematic representation of the physics behind the XPS [79]

XPS is a capable method to detect all elements except hydrogen and helium due to their small orbital diameter size. In the best of our knowledge, XPS is a common method for analyzing the inorganic compounds as well.

The physical background of the XPS is schematically represented in Figure 7. Dependent to the known energy of X-ray (obtained from the particular wavelength of the X-ray radiation) each emitted electron can be analyzed according to the equation:

$$E_{\text{binding}} = E_{\text{photon}} - (E_{\text{kinetic}} + \phi) \tag{2.6}$$

where E_{binding} is the binding energy (BE) of the electron, E_{photon} is the X-ray photon energy, E_{kinetic} is the kinetic energy of the electron measured, and ϕ is the work function of the spectrometer.

2.4.4 Electron microscopy

Electron microscopy is a very convenient method to investigate the specimen on a very small scale due to the highly energetic electron beam striking the specimen. The primary beam generates secondary and backscattered electrons, which are utilized in scanning electron microscopy (SEM), transmitted electrons, used in transmission electron microscopy (TEM), X-rays, detected in energy dispersive analysis, and diffracted electrons, employed in diffraction patterns. In the presence of this data, topographic, morphologic, compositional and crystallographic information can be easily analyzed. Figure 8 represents the primary beam and the generated electrons.

Scanning electron microscopy (SEM)

A scanning electron microscope is a kind of electron microscope that provides efficient information about the surface topography, composition, and other characteristic properties (e.g., electrical conductivity).

As mentioned before, two types of electrons are utilized to generate contrast in the images after the primary beam strikes the sample: backscattered electrons are generated by elastic scattering, and the secondary electrons by inelastic scattering. Morphological or, in other words, topographic information of a sample is achieved by trapping the secondary electrons originated from the surface, with Faraday cage as a secondary electron detector. The primary beam and the generated electrons are illustrated in Figure 8

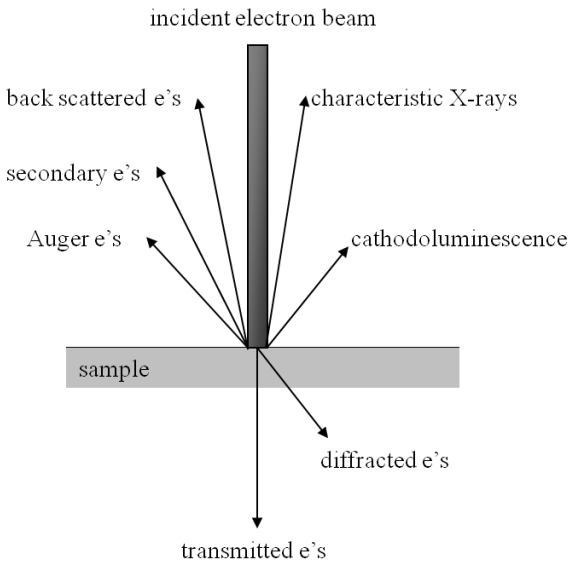

Figure 8. Illustration representing the main interactions of primary electron beam with a sample which is shown in gray.

Transmission electron microscopy (TEM)

One of the critical aspects of our study is to distinguish if the observed nanostructures are capsules or solid particle. Transmission electron microscopy allow us to achieve this morphological information from the images obtained when the beam is transmitted through our nanostructures. Darker parts of the TEM micrographs present denser or thicker regions due to the fewer electron transmission. Accordingly, the electrons can be transmitted easier through the core part of the capsules than through their walls.

Energy dispersive X-ray analysis (EDX)

In simple terms, energy-dispersive X-ray spectroscopy (EDX, EDS or EDAX) is capable to analyze the elemental content or chemical characterization of a sample by analyzing the characteristic X-rays emitted from the sample due to the inelastic interaction between primary electron beam and the specimen.

As also presented in the Figure 8, primary beam excite the inner shell electron followed by an electron movement from the higher shell to the vacancy. The energy difference of an electron from higher shell to the lower generates the X-ray radiation.

In our work, EDX was conducted to analyze the elemental analysis of the particle/capsule. The elemental content at the core and wall part of the capsules can be scanned by line scanning in two-dimensional spectrum images. Elemental mapping could provide the positions of the elements in a landscape. This method can also be performed to analyze the sample by three-dimensional images and to quantitatively analyze the elemental contents.

Chapter 3

Experimental procedures

3.1 Chemicals and materials

The following chemicals were used as purchased without further purification: cerium(III) nitrate hexahydrate ($Ce(NO_3)_3 \cdot 6H_2O$, Fluka), iron(III) chloride hexahydrate ($FeCl_3 \cdot 6H_2O$, Sigma–Aldrich), anhydrous iron(II) chloride ($FeCl_2$, Sigma–Aldrich), iron(II) sulfate heptahydrate ($FeSO_4 \cdot 7H_2O$, Fluka), toluene (Sigma–Aldrich, ≥99.7%), azobisisobutyronitrile (AIBN, Sigma–Aldrich), hexadecane (Sigma–Aldrich), a commercial polyisobutylene succinimide pentamine (referred to along the work as "Lubrizol U", Lubrizol Co., Rouen, France), polystyrene-*block*-poly(acrylic acid) with different chain length ratios (PS-*b*-PAA, ATRP Solutions, Inc., USA; Table 1 contains the molecular weights and polydispersity indices for the different PS-b-PAA copolymer used in the), sodium dodecyl sulfate (SDS, Roth, ≥99%), oleic acid (Sigma-Aldrich, 90%). triethylamine (Et_3N, Fluka, ≥99.5%), ethylenediamine (Sigma-Aldrich), tributhylamine (Bu_3N, Fluka, >98%), trimethylamine (Me_3N, Sigma-Aldrich), methylamine (MeA, Merk, 40% solution in water), sodium hydroxide (NaOH, Riedel-de Haën), and ammonia (NH_3, 28% solution in water). Styrene (S, Merck, 99%) was passed through an aluminum oxide column before use. Deionized water was used throughout the experiments.

Table 1. Polydispersity indices (PDI, M_w/M_n) and number average molar masses (M_n) of the corresponding block copolymers with different chain length ratios

	S_{50}-AA_{12}	S_{50}-AA_{23}	S_{60}-AA_{30}	S_{50}-AA_{90}	S_{50}-AA_{180}
PDI	1.16	1.13	1.1–1.3	1.15	1.12
M_n (g/mol)	6,100	6,900	6,500–9,130	11,600	18,200

3.2 Preparation of ceria nanocapsules in inverse (w/o) miniemulsion systems

Ceria nanocapsules were prepared by inverse miniemulsion according to the amounts of reagents presented in Table 2.The dispersed phase was prepared by dissolving $Ce(NO_3)_3 \cdot 6H_2O$ (2.6 mmol, 1.129 g) in water (2.0 g) and added into the continuous phase, which contains to-

luene (8.0 g) and the a polyisobutylene succinimide pentamine (Lubrizol U) and/or the PS-*b*-PAA copolymer as surfactants. The two phases were pre-emulsified by stirring with a magnetic stirrer for 1 h. Subsequently, the mixture was emulsified with an ultrasonicator (Branson Sonifier W450 digital, 1/2" tip, 4 min at 70% amplitude with a pulse of 1.0 s and a pause of 0.1 s) while cooling down in an ice–water bath. After the ultrasonic emulsification, the emulsion was further stirred for 1 h. Finally, Et_3N was added into the emulsion under constant stirring. The effect of the organic base on the ceria nanocapsule formation was examined by changing the amount of Et_3N from 544 to 1088 µL and varying the addition rate (cf. Table 2). Representative samples were washed with acetone, centrifuged (3000 rpm, 5 min) and dried in a vacuum oven at room temperature for 12–14 h. An analogous method was also used for corresponding samples without washing.

Table 2. Amounts of reagents and synthesis parameters for ceria nanocapsules by inverse miniemulsion. The dispersed phase was an aqueous solution of $Ce(NO_3)_3 \cdot 6H_2O$ with a constant concentration of 1.3 M in all cases. The continuous phase was prepared with the indicated amounts of the surfactants dissolved in 8.0 g of toluene.

Sample[(a)]	Continuous phase		Precipitating reagent	
	Lubrizol U [mg]	S_{50}-AA_{12} [mg]	Triethylamine (Et_3N) [µL]	Addition rate[(b)] [mL/min]
SV023-00	80.0	–	544	p.add.
SV023-07[(a)]	80.0	–	1088	~100
SV030-00	80.0	40	544	p. add.
SV028-02	80.0	–	544	~50
SV030-02	80.0	40	1088	p. add.
SV030-03	–	40	1088	p. add.
SV030-04	40.0	40	1088	p. add.

[(a)] For sample SV023-07, the triethylamine was dissolved in 500 mg of the continuous phase (a 1 wt% solution of Lubrizol U in toluene).
[(b)] p. add.: prompt addition (i.e., all at once) of the precipitation reagent.

3.3 Preparation of iron oxide nanocapsules in inverse (w/o) miniemulsion systems

The disperse phase was prepared by dissolving the appropriate iron salt ($FeCl_3 \cdot 6H_2O$, anhydrous $FeCl_2$, $FeSO_4 \cdot 7H_2O$, or a mixture of $FeCl_3 \cdot 6H_2O$ and $FeCl_2$) in water, according to the quantities reported in Table 3. The continuous phase contained Lubrizol U and/or S_{50}-AA_{12}. The mixture of the two phases was pre-emulsified by stirring for 1 h and ultrasonified afterwards (4 min, 70% amplitude, pulse: 1.0 s, pause: 0.1 s). The emulsified sample was stirred for 1 h. Finally, an organic base (Et_3N, ethylenediamine, or Bu_3N) was added while shaking continuously for 2 or 12 h by varying addition rates (cf. Table 3). Washing of representative samples was done as described in section 3.2.

Table 3 Amounts of reagents and synthesis parameters for iron oxide nanocapsules by inverse miniemulsions

Sample	Continuous phase (8.0 g of toluene)	Disperse phase[a, b]			Precipitating reagent			
	S_{50}-AA_{12}	$FeCl_3 \cdot 6H_2O$	$FeCl_2$	$FeSO_4$	Organic base			Addition rate[e]
					Et_3N	Ethylenediamine	Bu_3N	
	[mg]	[mmol]	[mmol]	[mmol]	[μL]	[μL]	[μL]	[mL/min]
SV025-00	–	–	2.6	–	544	–	–	p.add.
SV025-01			2.6		1088			~200
SV025-06	–	–	2.6	–	544	–	–	~100
SV025-03	–	1.56	1.04	–	1088	–	–	~200
SV026-00	–	–	2.6	–	–	521	–	~100
SV025-08[c]	–	1.56	1.04	–	1088	–	–	p.add.
SV025-16[c]	–	1.56	1.04	–	1088	–	–	p.add.
SV025-10	–	1.56	1.04	–	544	–	–	p.add.
SV029-00	40	–	2.6	–	544	–	–	p.add.
SV029-02	40	–	2.6	–	–	–	–	–
SV029-04[c]	40	–	2.6	–	1088	–	–	p.add.
SV029-10[b]	40	–	2.6	–	544	–	–	p.add.
SV029-11	40	1.56	1.04	–	1088	–	–	p.add.
SV029-12	40	1.56	1.04	–	–	–	1860	p.add.
SV029-13	40	1.56	1.04	–	–	372	–	p.add.
SV029-14	40	–	–	2.6	1088	–	–	p.add.

[a] Disperse phases were prepared by dissolving the metallic precursor(s) in 2.0 g of water.
[b] Differently from the samples, SV029-10 was prepared by using S_{50}-AA_{12} alone in the continuous phase, without Lubrizol U.
[c] The difference of these samples with respect to the others is the duration of shaking.
[d] p.add.: prompt addition (i.e., addition all at once) of the precipitating reagent

3.4 Preparation of iron oxide nanocapsules in direct (o/w) miniemulsion systems

3.4.1 Synthesis of iron-containing surface active agent

Ferrous dodecyl sulfate, $Fe(DS)_2$ was prepared by mixing aqueous solutions of SDS (0.1 M, 50 mL) and $FeCl_2$ (0.3 M, 50 mL) or $FeSO_4 \cdot 7H_2O$ (0.3 M, 50 mL). The mixture was kept in an ice–water bath and stirred on a magnetic stirrer until a white precipitate appeared. The precipitate, $Fe(DS)_2$, was filtered and dried in a vacuum oven at room temperature for 12–14 h.

3.4.2 Preparation of direct (o/w) miniemulsion systems

The disperse phase was prepared as a solution of PS-*b*-PAA (30.0 mg, with varying styrene-to-acrylic acid chain length ratios, as indicated in Table 4) in 785 mg of hexadecane or toluene. In an attempt to achieve better a stability of the droplet, hexadecane (5 wt% hexadecane in toluene) and oleic acid (2.63 mg in the disperse phase) were used. Continuous phases were prepared by dissolving SDS (88.5 mg) or $Fe(DS)_2$ (90.0 mg) in water (3.0 g) as additional surfactants. Reference miniemulsion samples were also prepared without these additional surfactants. Both continuous and disperse phases were stirred for 30 min separately and the mixture of the two phases was stirred for an additional period of 30 min. An aqueous solution of $FeCl_2$ (153 μL, 1.0 M) was also used as a metallic source in the presence of PS-*b*-PAA or SDS. The miniemulsion was achieved by ultrasonification (2 min, 70% amplitude, 1.0 s pulse, 0.1 s pause). Subsequently, given amounts of MeA or NH_3 were added at different addition rates (cf. Table 4). The resulting miniemulsions were shaken for 2 h.

3.5 Characterization techniques

XRD measurements were performed in a Philips PW 1820 diffractometer by using $Cu_{K\alpha}$ radiation (λ = 1.5418 Å) in the range 2θ = 0–70°. Samples were typically measured before and after washing.

Scanning electron microcopy (SEM) micrographs were acquired by using a LEO 1530 Gemini microscope. Energy-dispersive X-ray (EDX) spectroscopy analysis was performed in

a Hitachi SU8000 scanning electron microscope. For SEM and EDX measurements, samples were prepared by diluting the resulting miniemulsion samples in water or toluene, depending on the continuous phase used in the experiments, and drop-casting on a silicon wafer.

Transmission electron microscopy (TEM) micrographs were taken by using a Zeiss EM912 or a JEOL JEM 1400 microscope. Samples were prepared by dropping dilutions of the samples in water or toluene on carbon-coated copper grids.

In the case of the inverse miniemulsion samples containing PS-*b*-PAA as a surfactant, the samples were further calcinated at 600 °C (from room temperature to 600 °C with a heating rate of 5 °C/min; plateau of 1 h at 600 °C).

Particle size histograms and their distributions were obtained by measuring the sizes of at least 100 capsules from corresponding SEM or TEM micrographs with the help of the software ImageJ.

Magnetic measurements were carried out with a custom-built vibrating sample magnetometer (VSM), (H_{max} = 8000 Oe). Moment detectors are assembled as four pieces of coil, from Lakeshore. All the samples were measured as a powder, before and after washing.

Thermogravimetric analysis (TGA) was carried out in a Mettler ThermoSTAR TGA/SDTA 851 thermobalance. TGA of the surfactants described in chapter 3.4.2 was done under an oxygen atmosphere with a temperature range from room temperature to 1200 °C at 10 °C/min. For samples described in chapter 3.2, 3.3, and 3.4, the measurements were carried out under a nitrogen atmosphere, in the range from room temperature to 1000 °C at 10 °C/min. The measurements were performed for powder samples before and after washing.

XPS of the powders samples was investigated with a Perkin-Elmer Φ 5600-ci instrument using standard Al-K_α radiation (1486.6 eV) operating at 350 W. The working pressure was $\leq 5 \cdot 10^{-8}$ Pa ($\sim 10^{-11}$ Torr). The calibration was based on the binding energy (BE) of the $Au4f_{7/2}$ line at 83.9 eV with respect to the Fermi level. The standard deviation for the BE values was 0.15 eV. The reported BE values were corrected for the BE charging effects, assigning the BE value of 284.6 eV to the C1s line of carbon. Survey scans were obtained in the range 0–1350 eV (pass energy 187.5 eV, 1.0 eV/step, 25 ms/step). Detailed scans (58.7 eV pass energy, 0.1 eV/step, 50–150 ms/step) were recorded for the O1s, C1s, N1s, Fe2p, FeLMM, regions. The atomic composition, after a Shirley-type background subtraction, was evaluated using sensitivity factors supplied by Perkin-Elmer. Charge effects were partially compensated by using a charge neutralizer (flood gun). Peak assignment was carried out according to literature data.

Table 4. Amounts of reagents and synthesis parameters for direct miniemulsion systems in the presence of S_x-b-AA_y as a surfactant

Sample	Continuous phase (3.0 g of water)		Disperse phase						Free metal ion addition	Precipitating reagent		
	$Fe(DS)_2$	SDS	S_x-*b*-AA_y				Oleic acid	Hydro-phobic medium[a]	$FeCl_2$ (aq) 1.0 M	Base 5.0 M		Addi-tion rate[b]
			S_{60}-AA_{30}	S_{50}-AA_{23}	S_{50}-AA_{90}	S_{50}-AA_{180}				MeA	NH_3	
	[mg]	[mg]	[mg]	[mg]	[mg]	[mg]	[mg]		[µL]	[µL]	[µL]	[µL/min]
SV021-03	90	–	30	–	–	–	2.63	HD	–	–	460	p.add.
SV021-04	–	–	30	–	–	–	–	HD	153	–	612	p.add.
SV021-05	–	88.5	30	–	–	–	–	T	51	276	–	p.add.
SV021-07	–	88.5	30	–	–	–	–	T	153	–	276	p.add.
SV021-13	–	88.5	–	30	–	–	–	T	153	460	–	92
SV021-14	–	88.5	–	–	30	–	–	T	153	460	–	92
SV027-04	90	–	–		–	30	2.63	HD	–	–	460	92
SV021-12	–	88.5	–	30	–	–	–	T/HD	153	–	276	92

[a] As hydrophobic media, toluene (T), hexadecane (HD), hexadecane and styrene (HD/S), toluene and 5 wt% of hexadecane (T/HD) were used.
[b] p.add.: prompt addition (i.e., all at once) of the precipitating reagent

Chapter 4

Interfacial crystallization in inverse miniemulsion systems

The literature provides many successful applications of iron oxide nanoparticles in a wide range of disciplines, including magnetic fluids,[80] catalysis,[81-82] biotechnology and biomedicine,[83] magnetic resonance imaging,[84-85] data storage,[86] and environmental remediation.[87-88] Much research has also been devoted to the application of cerium dioxide in fields such as catalysis, electrochemical cells, ionic conduction, and UV optical filtrations.[89] In our study, interfacial crystallization of cerium and iron oxides was achieved in inverse miniemulsion systems. This work focuses on the application of soft template methods, which have not been previously used for the preparation of ceria or iron oxide nanoparticles. Figure 9 represents schematically the miniemulsion procedure used to drive crystallization to the droplet interface. In a typical synthesis, an aqueous solution of the metallic precursor was used as a disperse phase and mixed with an organic phase containing the polymeric surfactant(s). An organic base was added after the ultrasonic emulsification to induce the metal oxide precipitation.

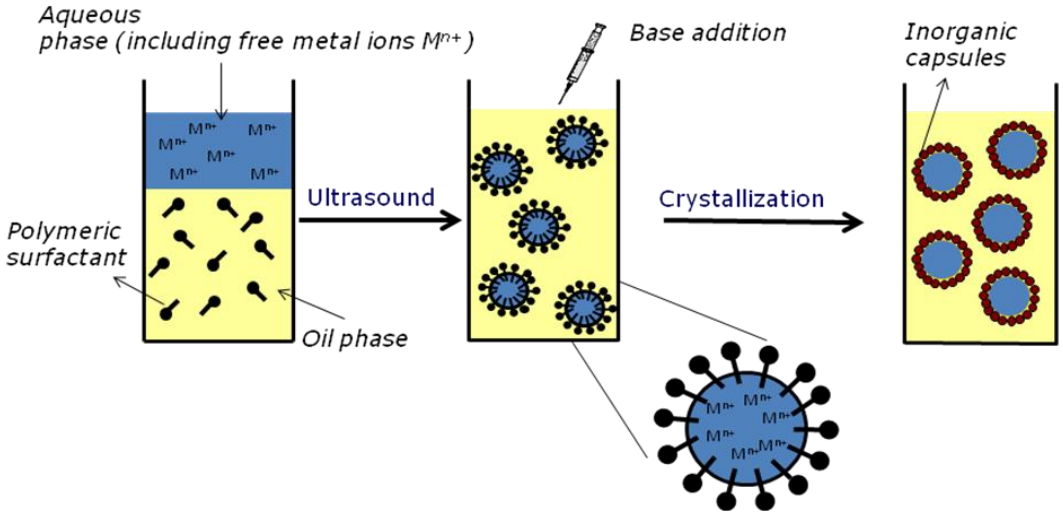

Figure 9. Schematic representation of interfacial crystallization in inverse miniemulsion systems.

The influence of different synthetic parameters on the capsule formation was investigated. First, the use of a commercial polyisobutylene succinimide pentamine (Lubrizol U) and PS-*b*-

AA as polymeric surfactants was compared. The chemical structures of these surfactants can be found in Scheme 2. Second, the amount and the chemistry of the bases were shown to have a significant effect on the results. Moreover, the influence of the metallic precursor type was also examined for the case of iron oxides.

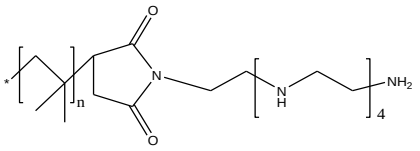

polyisobutylene succinimide pentamine
(Lubrizol U)

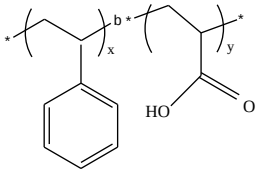

polystyrene-*block*-poly(acrylic acid)
(PS-*b*-PAA)

Scheme 2

4.1 Interfacial crystallization of cerium oxide

Interfacial crystallization of polycrystalline ceria (CeO_2) was achieved under ambient conditions without any further thermal treatment. $Ce(NO_3)_3 \cdot 6H_2O$ was used as a metallic precursor in aqueous phase and the concentration of Ce^{3+} ions was kept constant at 1.3 mol/L.

Effect of surfactant type and amount

Lubrizol U has been shown in previous works to be a very effective surfactant in w/o systems.[90-91] However, in the context of the crystallization at the droplet interface, it would be highly desirable to use an amphiphilic block copolymer, such as PS-*b*-PAA, containing functional groups able to bind metals.[92] Therefore, we studied the differences between the use of Lubrizol U and S_{50}-AA_{12}. We compared samples prepared with only Lubrizol U (80.0 mg), Lubrizol U (80.0 mg) and S_{50}-AA_{12} (40 mg), and only S_{50}-AA_{12} (40 mg). Moreover, a fourth sample was also prepared with less amount of Lubrizol U and S_{50}-AA_{12} (40 mg of each surfactant). All the other synthetic parameters were kept constant in these four samples. An overview of these samples and their properties is contained in Table 5.

Table 5. Summary of the effects of surfactant type and amount on the interfacial crystallization of ceria. Each sample contains 8.0 g of toluene with the indicated amounts of dissolved polymeric surfactants as a continuous phase and the amount of dispersed phase was kept constant. (cf. Table 2)

Sample	Lubrizol U [mg]	S_{50}-AA_{12} [mg]	SEM/TEM (morphology)
SV023-07	80	–	capsular
SV030-02	80	40	solid particles/sporadic capsules
SV030-03	–	40	solid particles/sporadic capsules
SV030-04	40	40	solid particles/sporadic capsules

Figure 10 presents the SEM and TEM micrographs of samples prepared with different contents of these surfactants. The most remarkable influence is the morphological changes of the particles, as shown in the electron micrographs of Figure 10. The presence of Lubrizol U without any block copolymer results in a capsular morphology (Figure 10 (A)). Surprisingly, when the same amount of Lubrizol U and S_{50}-AA_{12} is used (Figure 10 (B)), solid particles with only sporadic occurrence of capsules were formed. The hydrophilic part (acrylic acid) of the block copolymer locates inside the water droplets and complexes the cerium ions due to the metal-binding ability of the carboxylic groups. Subsequently, the nuclei formation and crystal growth may take place inside these droplets rather than at the interfaces. Hence, the crystallization process might lead to the formation of solid particles. As judged from the rough surface and the contrast difference observed in the SEM and TEM images, respectively, the presence of the block copolymer may promote the formation of porous particles. No observable morphological changes were detected by changing the amount of Lubrizol U (Figure 10 (B)–(D)).

Differently from the results obtained previously with soft template methods,[49-50] in which amorphous materials were obtained, in this work we were able to achieve polycrystalline nanoparticles after base addition without any further thermal treatment. The results from electron diffraction (diffraction patterns presented in the last column of Figure 11) were consistent with those obtained by X-ray diffraction (presented in Figure 11) and indicated the presence of polycrystalline ceria.

XRD patterns of the sample prepared with only Lubrizol U before washing (Figure 11 (E)) shows the reflections of cubic CeO_2 (JCPDS Card No. 34-0394). The patterns of the sample prepared with only S_{50}-AA_{12} (Figure 11 (A)) shows, besides cubic-CeO_2, the presence of triethylammonium chloride (JCPDS Card No. 38-1974), which is a by-product of the precipitation reaction. Interestingly, the use of a mixture of S_{50}-AA_{12} and Lubrizol U results

on reflections that can be identified neither to triethylammonium chloride nor to cubic-CeO_2 (Figure 11 (B)).

After washing with acetone, only the reflections of cubic CeO_2 were observed for all samples (the reflection at $2\theta = 38.3°$ corresponds to the specimen holder).

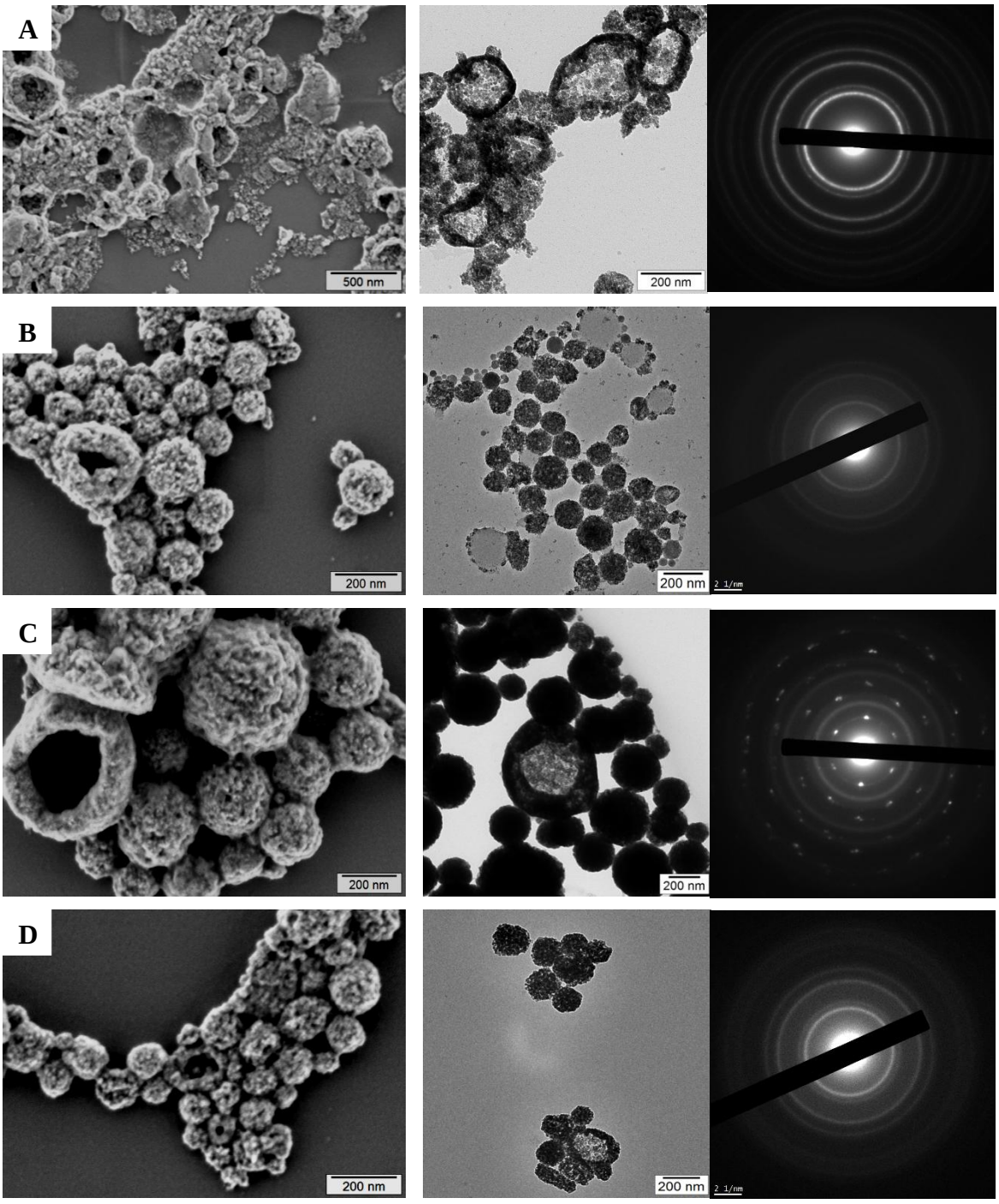

Figure 10. SEM and TEM micrographs and corresponding diffraction patterns of samples prepared in the presence of (A) 80.0 mg Lubrizol U (B) 80.0 mg Lubrizol and 40.0 mg S_{50}-AA_{12} (C) 40.0 mg S_{50}-AA_{12} and (D) 40.0 mg Lubrizol U and 40.0 mg S_{50}-AA_{12} (samples SV023-07, SV030-02, SV030-03 and SV030-04 of Table 5, respectively).

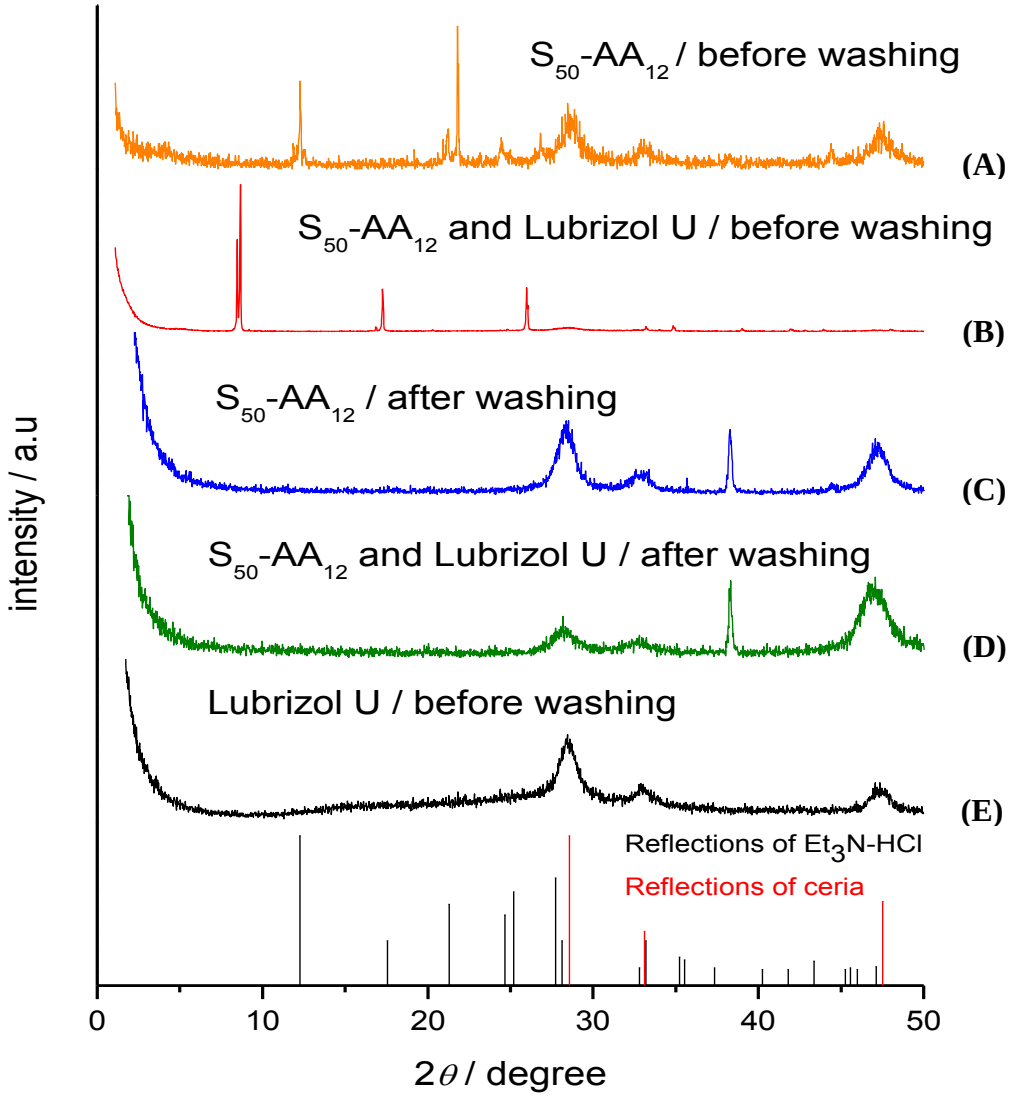

Figure 11. X-ray diffraction patterns of samples with different surfactant content, before and after washing, presented with characteristic reflections of ceria and Et_3N–HCl.

To get further information about the chemical composition of single capsules, a sample prepared with Lubrizol U and S_{50}-AA_{12} (sample SV030-00 of Table 5) was analyzed by energy-dispersive X-ray spectroscopy (EDX).

The EDX analysis corresponding to a single capsule is shown in Figure 12. High-intensity peaks of cerium, oxygen, and carbon, which are the elements constituting the capsule, along with a weak silicon peak from the wafer are observed. The peaks of Ce and O correspond to ceria, and the peak of C indicates the presence of polymeric surfactants remaining in the capsule. The EDX line analysis shown in Figure 12(B) indicates higher counts of cerium, oxygen and carbon along the walls of the capsule.

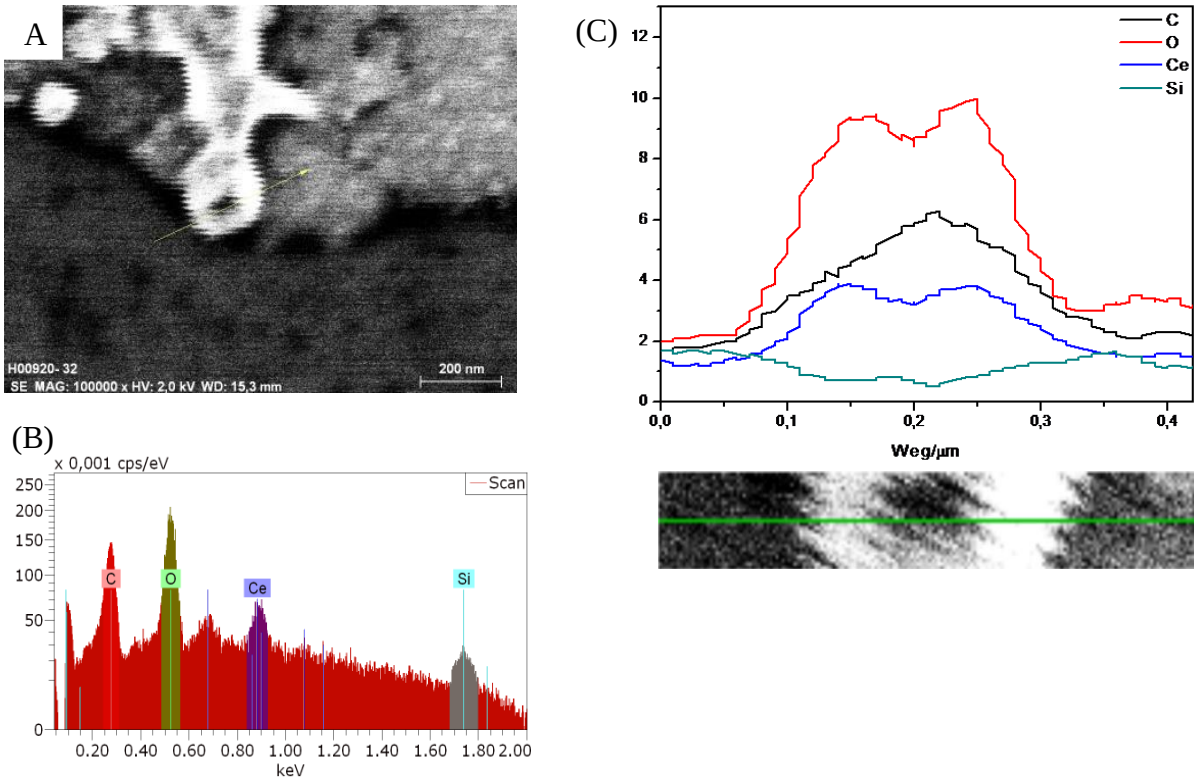

Figure 12. (A) SEM micrograph of the analyzed region for EDX. (B) Energy-dispersive X-ray spectroscopy of the sample. (C) EDX line analysis of the sample with corresponding SEM micrograph.

Additionally, elemental compositions of the samples containing only Lubrizol U and Lubrizol U/S_{50}-AA_{12} were investigated by X-ray photoelectron spectroscopy (XPS). In Figure 13, the survey spectrum of the sample containing only Lubrizol U is plotted; all transitions of the species of interest (Ce, O, C) can be clearly seen.

The atomic percentages of the elements, reported in Table 6, were calculated from some of the collected detailed spectra of the main photoelectron lines (C1s, O1s, Ce3d).

Table 6. Atomic percentages delivered by XPS analysis of the samples.

Sample	Surfactant(s)	%O	%Ce	%C	O/Ce
SV023-00	Lubrizol U	33.0	2.3	64.7	14.3
SV030-00	Lubrizol U / S_{50}-AA_{12}	28.3	1.8	69.8	15.7

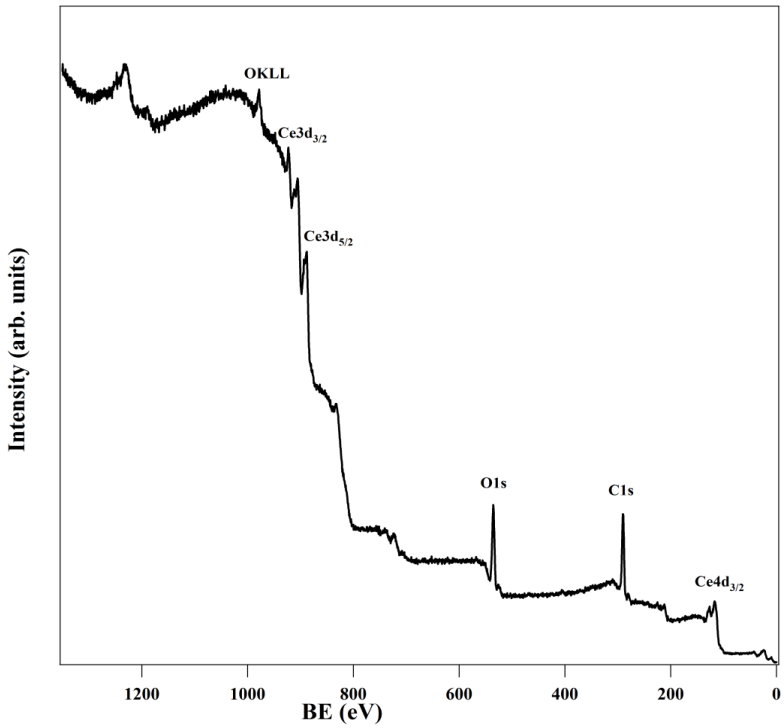

Figure 13. Survey spectra of the sample with only Lubrizol U as a polymeric surfactant.

Some main conclusions can be drawn from the XPS data:

1. The carbon content on the surface of both powders is relevant (60% atomic), which may be ascribed to the presence of surfactant molecules on the surface of ceria nano-particles, but also to remaining triethylammonium chloride.
2. The amount of oxygen, quite high on the sample surface, and remarkably higher (14.3 and 15.7, see Table 6) than the expected O/Ce atomic ratio (i.e., 2 in Ce_{O2}) can be ascribed to the presence of the surfactant.
3. The amount of cerium appears to be low, which can be explained by the fact that the first investigated layers are those of the surfactant coating.

As far as the chemical state of the different species is concerned, which can be evaluated by the binding energy (BE) values of the main regions, the BE values for the different species (all corrected for charging effects by assigning to the C1s the reference value of 284.6 eV) are reported in Table 7.

Table 7. BE values of the O1s and Ce3d lines, together with the experimentally determined Auger parameters (values corrected for charging effects)

Sample	Surfactant(s)	BE O1s I (eV)	BE O1s II (eV)	BE Ce3d (eV)
SV023-00	Lubrizol U	529.4	531.2	882.1
SV030-00	Lubrizol U / S_{50}-AA_{12}	529.2	531.4	882.3

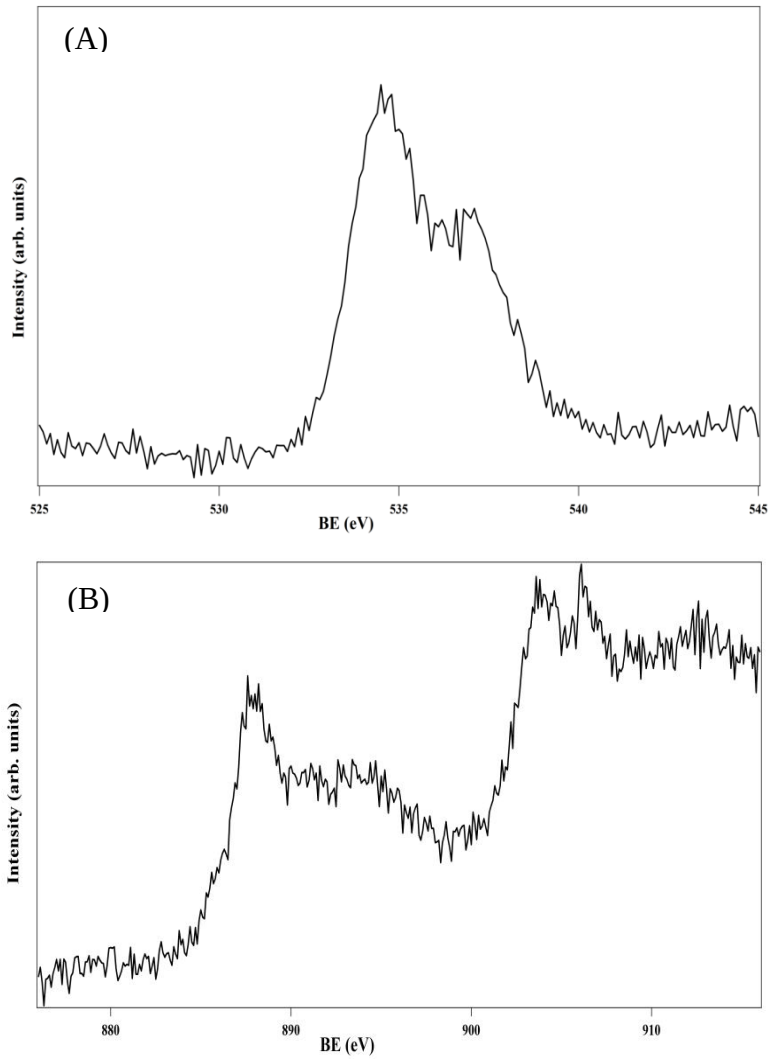

Figure 14. (a) O1s region and (b) Ce3d region of the sample containing only Lubrizol U as a surfactant

The oxygen main region, O1s, clearly shows two components (see Figure 14(A)), the first one, at lower BE (about 529.2-529.4 eV), which could be ascribed to ceria, the second one to the surfactant moieties. Concerning cerium, the main peak, Ce3d, presents a complicated shape (see Figure 14(B)), with the presence of satellite peaks and further features, which can hint at the presence of different chemical environments or oxidation states. A preliminary analysis of the BE shows, for the main peak, a value of 882.1 eV for the sample containing only Lubrizol U and of 882.3 eV for the sample which prepared by Lubrizol U/S_{50}-AA_{12}, which are values typical of Ce(IV) in ceria.

Morphological changes due to decomposing the block copolymer by thermal treatment were also investigated. For this purpose, a sample including both Lubrizol U and S_{50}-AA_{12}, was calcinated at 600 ºC. The thermogravimetric analysis shown in Figure 15(A) exhibits that; no further weight loss can be observed above 480 °C, indicating that the polymeric surfactant has completely decomposed. After calcination at 600 °C, no distinctive change was

observed on capsular morphology, although all the polymeric content is removed (Figure 15(B)).

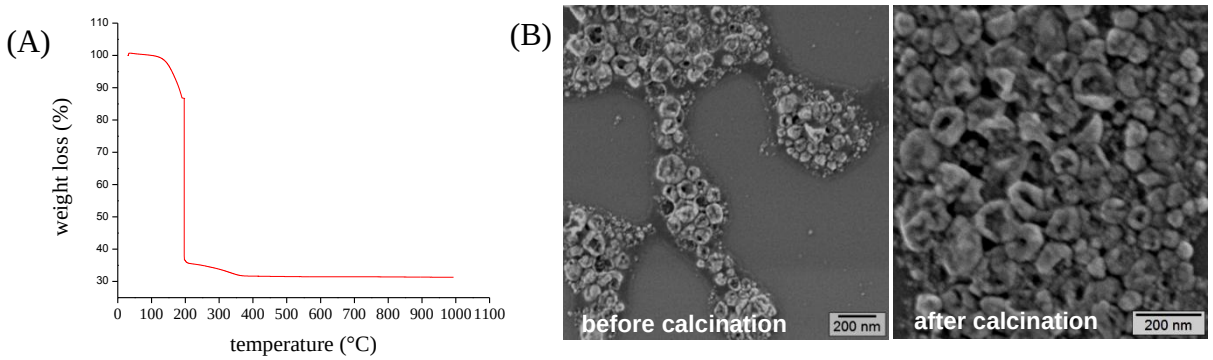

Figure 15. (A) Weight loss as a function of the temperature for the sample in the presence of Lubrizol U and S_{50}-AA_{12} before washing. SEM micrographs of the same sample (B) before and after calcination (cf. sample SV030-00 of Table 2).

Effect of organic base type and amount

Organic bases, the variable amounts used, addition rates and their effects on the resulting samples are listed in Table 8. Samples were prepared in the presence of only Lubrizol U as a surfactant, keeping constant the other synthetic parameters.

Table 8. Organic bases used to form ceria nanocapsules and their effects on capsule sizes.

Sample[(a)]	Precipitating reagent[(b)]			Addition rate[(c)]	Size
	Et_3N	Bu_3N	Me_3N		
				[mL/min]	[nm]
SV023-00	1:1.5	–	–	p.add.	~90
SV028-02	1:1.5	–	–	~50	~90
SV023-07	1:3.0	–	–	~100	~175
SV023-02	–	–	1:1.5	p.add.	~100
SV030-07	–	1:3.0	–	p.add.	~150

[(a)] Precipitating reagent was prepared as a solution in 500 mg of continuous phase for samples SV028-02, SV028-07 (toluene+1wt% Lubrizol U).
[(b)] Amounts of the represented bases are indicated as Ce^{3+}-to-organic base mol ratios.
[(c)] P.add.: prompt addition (i.e., all at once) of the precipitating reagent

First of all, by keeping constant the amounts of Et_3N, the effect of the addition rate was investigated by adding the bases all at once (promptly) and with a rate of 50 mL/min. All the other synthetic parameters were kept constant. SEM micrographs presented in Figure 16 show that the addition rate has no significant effect on the morphology.

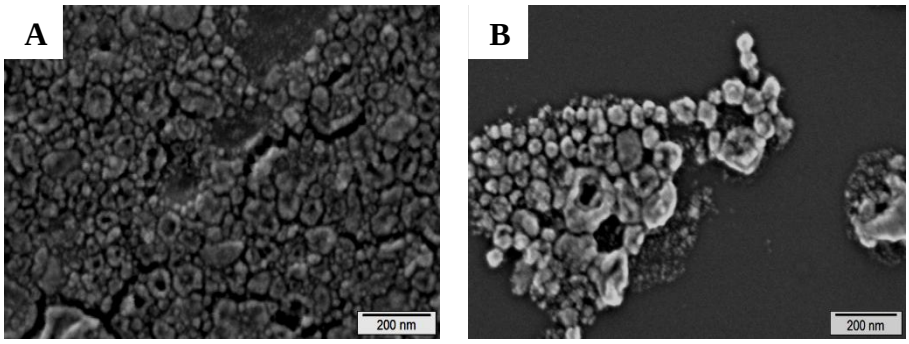

Figure 16. SEM micrographs of samples which were prepared by addition of Et_3N with different addition rates as (A)prompt, (B) ca. 50 mL/min (samples SV023-00 and SV028-02 of Table 8, respectively).

Secondly, the influence of the base amount was studied by varying the Ce^{3+}-to-Et_3N molar ratio from 1:1.5 to 1:3.0. TEM micrographs and the corresponding electron diffraction patterns, shown in Figure 17, demonstrated the formation of polycrystalline ceria nanocapsule for both samples in the presence of different base amounts. It is known that the colloidal particle size and the porosity of the resulting materials can be influenced by the pH value due to changes in hydrolysis and condensation.[93] Corresponding particle size histograms in Figure 17 clearly show that relatively larger ceria nanocapsules were achieved in the presence of higher amount of Et_3N.

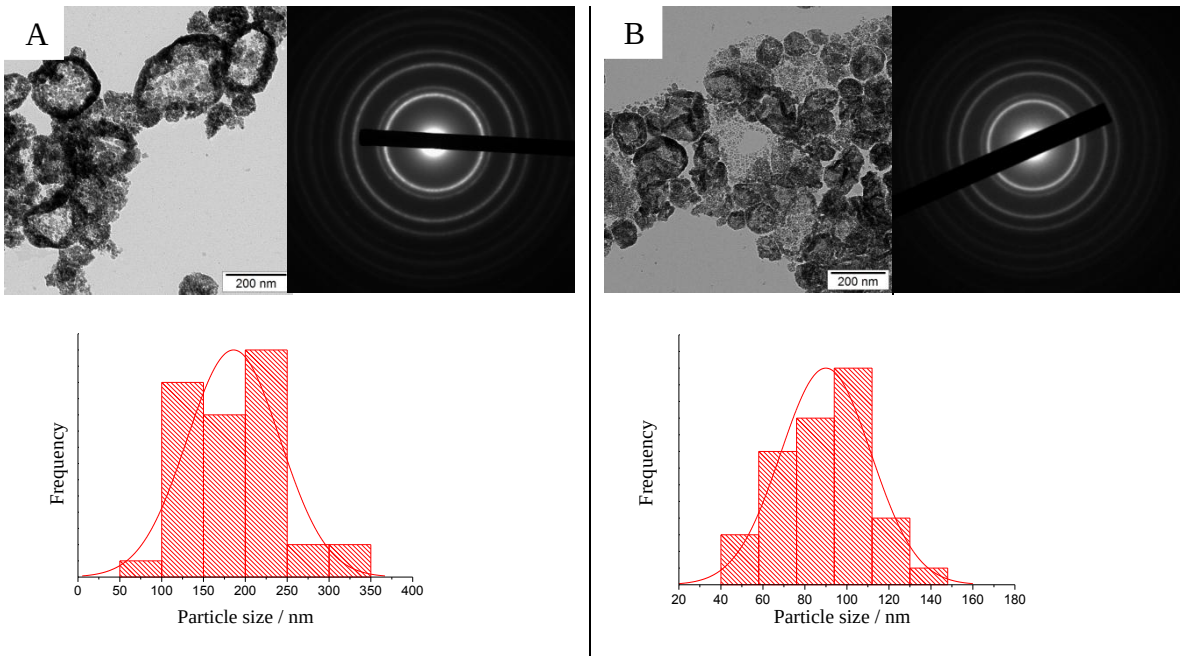

Figure 17 TEM micrographs with corresponding diffraction patterns of ceria nanocapsules in the presence of (A) Ce^{3+}-to-Et_3N mol ratio of 1:3.0 and (B) Ce^{3+}-to-Et_3N mol ratio of 1:1.5 as organic base (miniemulsion samples SV023-07 and SV023-00 of Table 8, respectively).

Triethylamine was used in the precipitation of zirconium and hafnium hydroxides at the droplet interface, recently reported in our group.[50] In this section, the influence of the precipitating reagent type was examined by comparing three tertiary amines, whose chemical structures are shown in Scheme 3: trimethylamine (Me_3N), triethylamine (Et_3N) and tributhylamine (Bu_3N).

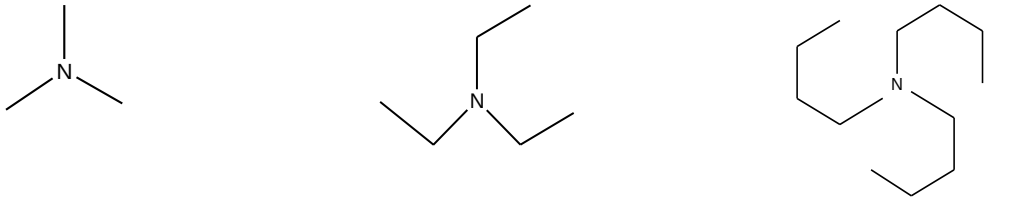

trimethylamine (Me_3N) triethylamine (Et_3N) tributhylamine (Bu_3N)

Scheme 3

SEM micrographs of the prepared samples are presented in Figure 18. It has been already indicated that hollow particles of ceria were observed in presence of Et_3N, but micrographs in panels (B) and (D) of Figure 18 show that crystallization of ceria can also be driven to the interfaces of droplets in presence of Me_3N and Bu_3N. No significant change in the size and morphology of the capsules was detected when using bases with different alkyl chains.

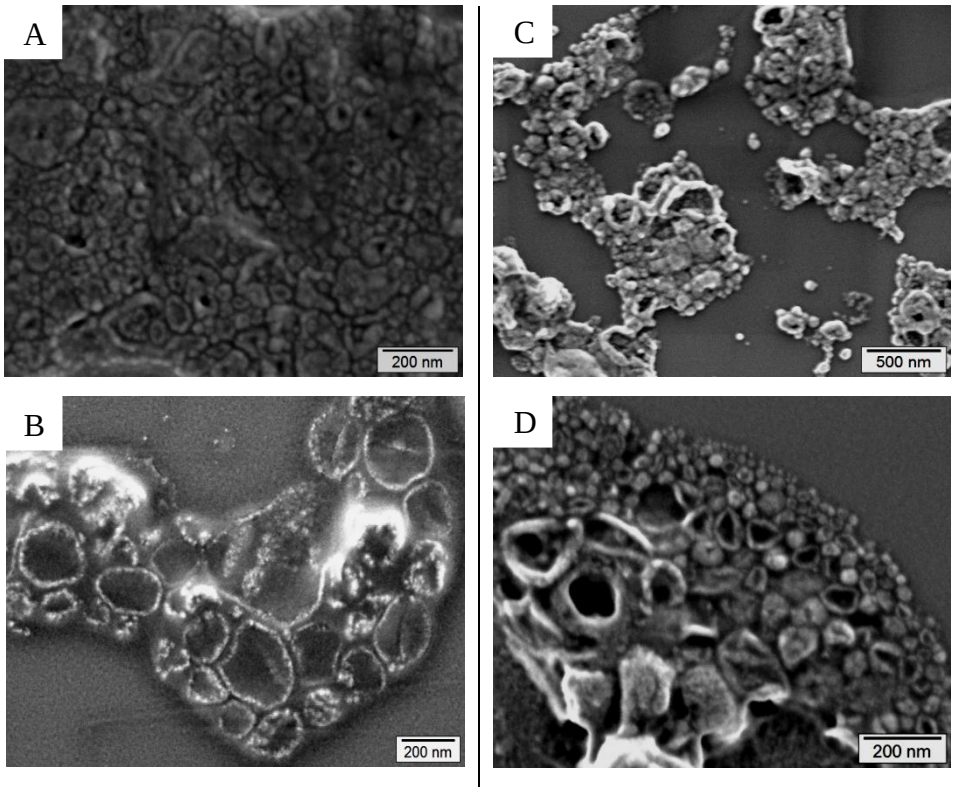

Figure 18. SEM micrographs of the samples which were prepared by addition of (A) Et_3N, (B) Me_3N with a Ce^{3+}-to-amine mol ratio of 1:1.5 and (C) Et_3N, (D) Bu_3N with a Ce^{3+}-to-amine mol ratio of 1:3.0. (Samples SV023-00, SV023-02, SV023-07, and SV030-07 of Table 8, respectively).

In summary, a change in the size of the ceria nanocapsules was only observed by changing the organic base amount rather than by using different amines at constant concentration. Higher amount of Et_3N resulted in larger size capsule formation. A tentative explanation for these observations may be that, at higher base concentration, there is enough base to complete the oxide shell formation around droplets of bigger size; if the base is not sufficient to precipitate enough oxide to cover the big droplets, only smaller particles would be formed.

4.2 Interfacial crystallization of iron oxide

Much research has been devoted to synthesize iron oxide hollow spheres by inverse miniemulsion[94-96], yet none of these studies have achieved polycrystalline and highly magnetic iron oxide nanosized capsules at ambient conditions without any further treatment. In this section, the type of surfactant, organic base and metal precursor, as well as the variation of their amounts were screened to investigate the changes on morphology and properties of the resulting iron oxide particles/capsules.

Effect of surfactant type

As previously done for ceria, the effect of the type and amount of surfactant was also examined for the case of iron oxide. An overview of the samples prepared to study the influence of the surfactant type on the iron oxide formation, together with their main properties, is shown in Table 9.

Table 9. Summary of the effects of surfactant type on the interfacial crystallization of iron oxides. Each sample contains 8.0 g of toluene with the indicated polymeric surfactants as a continuous phase and dispersed phases were prepared in presence of the metallic precursors denoted in the table. (cf. Table 3)

Sample	Precursor(s)	Surfactant(s)	Size, nm	Magnetic properties[(a)]	Morphology
SV025-08	Fe^{2+}/Fe^{3+}	Lubrizol U	~200	s. paramagn. (higher)	capsular
SV029-11	Fe^{2+}/Fe^{3+}	Lubrizol U/S_{50}-AA_{12}	~165	s. paramagn. (lower)	capsular
SV029-04	Fe^{2+}	Lubrizol U/S_{50}-AA_{12}	~140	–	capsular (poor)
SV029-10	Fe^{2+}	S_{50}-AA_{12}	~1000	–	capsular

[(a)] The magnetic properties column represents the magnetic behaviors of the samples and qualitative magnetization comparison of the corresponding samples to each other under the same magnetic field. s. paramagn.: superparamagnetic.

First, the screening of the surfactant type was carried out for samples prepared with a mixture of Fe(II) and Fe(III). Figure 19(A) and (B) present the electron micrographs of samples prepared with only Lubrizol U and with a mixture of Lubrizol U and S_{50}-AA_{12}. Another group of samples containing only Fe(II) as a metallic precursor was also synthesized in presence of Lubrizol U (Figure 19(C)) and S_{50}-AA_{12} (Figure 19(D)).

As shown in panels A and B of Figure 19, the presence of Lubrizol U with and without block copolymer led to the formation of crystalline iron oxide nanocapsules in the case of precursors with Fe^{2+} and Fe^{3+} ions and no significant differences were observed. When we compare the images of the samples with only Fe^{2+}, we can detect a significant difference on the resulting morphology when the surfactant content is changed, as shown in panels C and D of Figure 19. The mixture of Lubrizol U and S_{50}-AA_{12} results in hollow particles with a poor shape (see panel C of Figure 19). The sample prepared with only S_{50}-AA_{12} showed one of the most efficient capsules formation (see panel D of Figure 19); the larger capsule size of this sample is also remarkable. The corresponding size distributions are shown in the Figure 20.

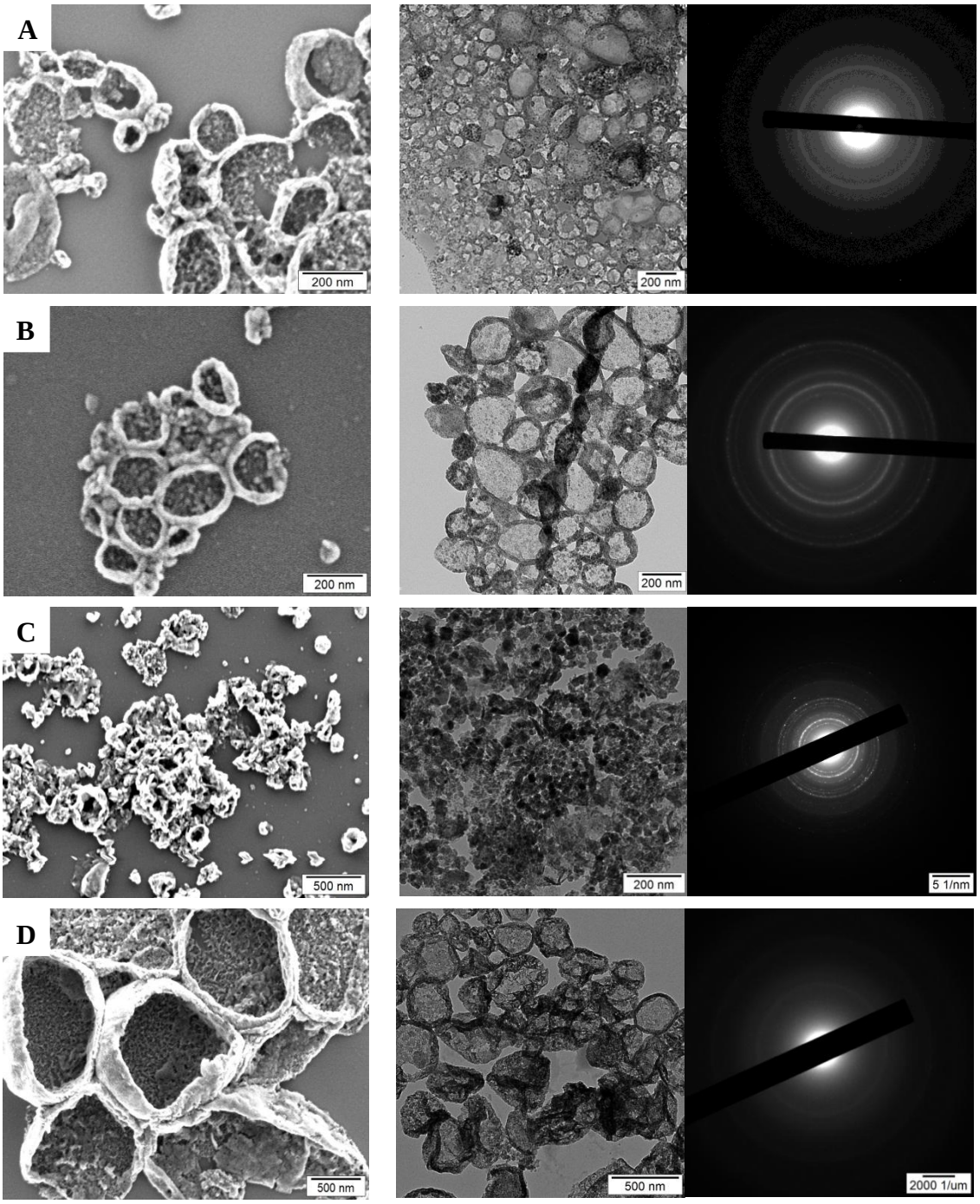

Figure 19. SEM and TEM micrographs and corresponding diffraction patterns of samples prepared in the presence of (A) 80.0 mg Lubrizol U (B) 80.0 mg Lubrizol U and 40.0 mg S_{50}-AA_{12}, (C) 80.0 mg Lubrizol U and 40.0 mg S_{50}-AA_{12} and (D) 40.0 mg S_{50}-AA_{12} as surfactant.(samples SV025-08, SV029-11, SV029-04 and SV029-10 of Table 9, respectively). Fe^{2+} and Fe^{3+} ions were used as metallic precursors for sample SV025-08 and SV029-11, Fe^{2+} ions were used as a metallic precursor for sample SV029-01 and SV029-10.

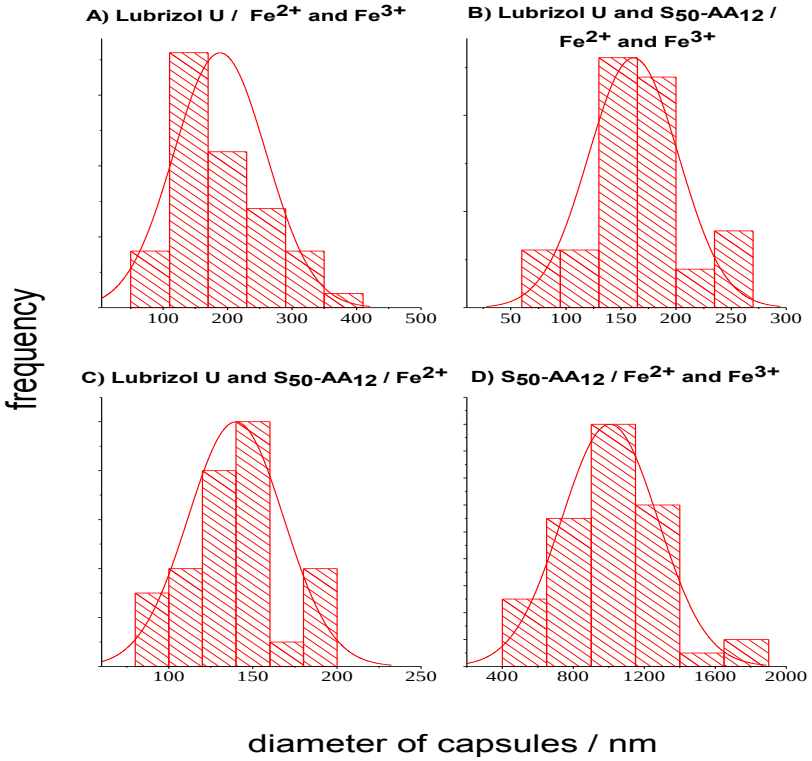

Figure 20. Particle size histograms for whose SEM/TEM and diffraction patterns were shown in Figure 19 (the letters shown in the figure correspond to the same letters in Figure 19).

XRD measurements were conducted to analyze the crystal structure of the samples prepared with Lubrizol U, S_{50}-AA_{12}, and a mixture of both. XRD patterns in Figure 21 show the presence of triethylammonium chloride (JCPDS Card No. 38-1974) in the unwashed samples. After washing, reflections that can be ascribed to magnetite (JCPDS Card No. 19-0629) or maghemite (JCPDS Card No. 39-1346) are found in all patterns, but triethylamine hydrochloride is still present. Reflections occasionally seen at 2θ values of 38° and 44° correspond to the aluminum sample holder.

Similarly to the results presented for ceria in section 4.1, the elemental content of a single capsule was analyzed by electron-dispersive X-ray spectroscopy (EDX). Figure 22 shows the analysis of a sample prepared with Lubrizol U as a surfactant and with a mixture of Fe^{2+} and Fe^{3+} as a metallic source.

EDX spectra in Figure 22(B) corresponds to the capsule which is shown in Figure 22(A), contains high-intensity peaks of iron, oxygen and carbon, with a silicon peak that belongs to the silicon wafer. Taking into account the XRD results presented before (see Figure 21), we can assume that the iron and oxygen peaks are due to magnetite or maghemite. The carbon peak is ascribable to the presence of Lubrizol U.

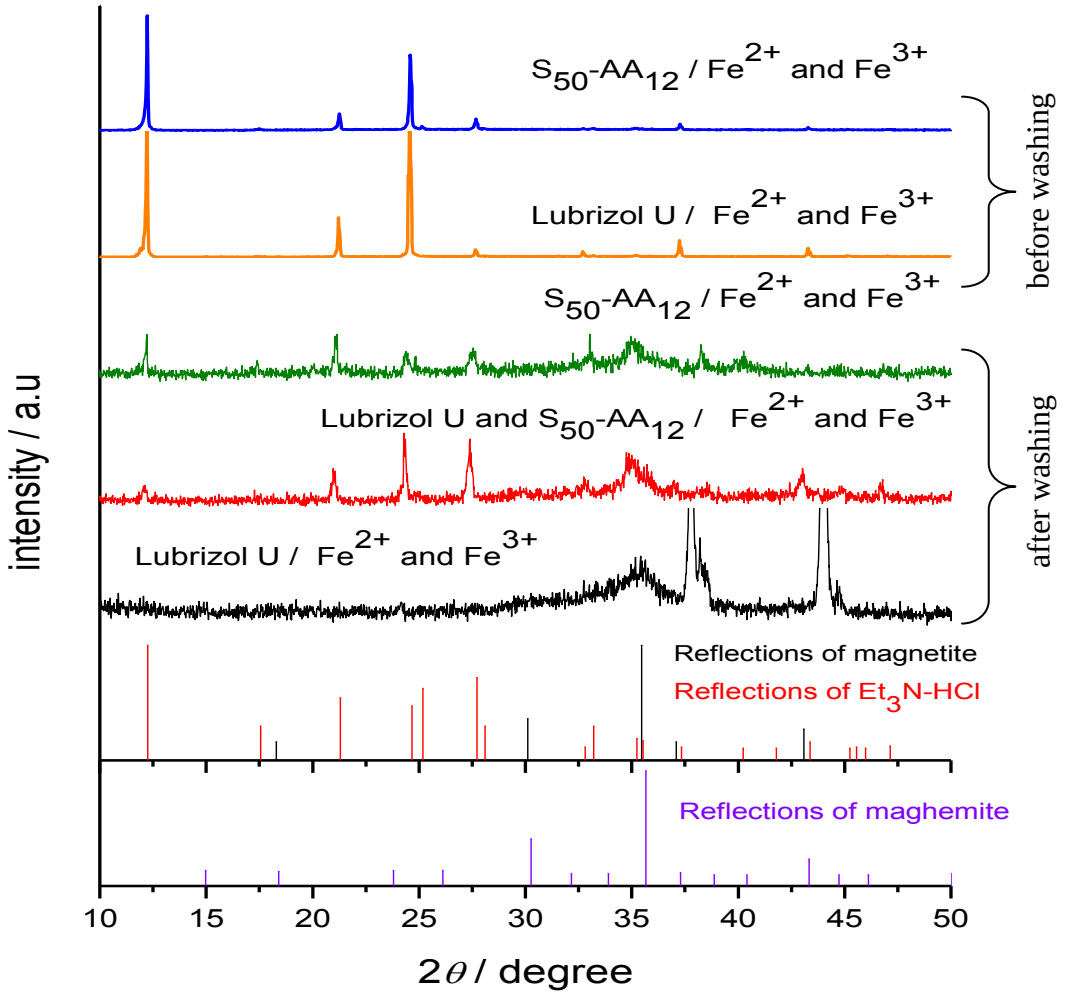

Figure 21. X-ray diffraction patterns of samples with different surfactant and metallic precursor content, before and after washing. The vertical lines which indicate the positions and relative intensities of reflections of magnetite, maghemite and Et_3N-HCl (The represented samples are: (i) SV029-10 (before washing) (ii) SV025-08 (before washing), (iii) SV029-10 (after washing), (iv) SV029-11 (after washing), (v) SV025-08 (after washing) in an order from the first column to the fifth. cf. Table 9).

The EDX line analysis of the sample (Figure 22 (C)) shows the distribution of iron, oxygen and carbon along the green arrow crossing the capsule as indicated in the SEM image below. A higher mass content of carbon, oxygen, and iron was detected at the walls of the capsule. Elemental mapping, shown in Figure 23, allowed us to analyze the elemental distribution. As expected, C, Fe, and O is mainly detected in walls of the capsules.

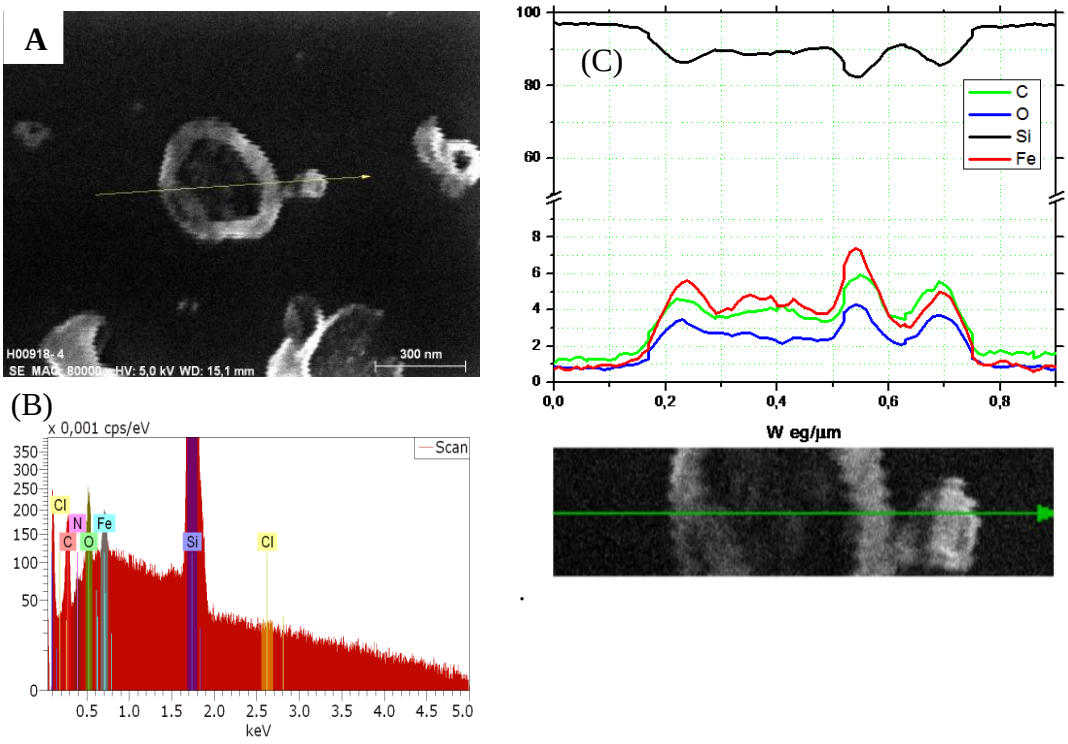

Figure 22. (A) SEM micrograph of the analyzed region for EDX analyze. (B) Energy-dispersive X-ray spectroscopy of the sample. (C) EDX line analysis of the sample with corresponding SEM micrograph below. (cf. sample SV025-08 of Table 9)

It is expected that nanosized hollow spheres present superparamagnetism.[97-99] Hence, the magnetic properties of the samples were examined in a vibrating sample magnetometer (VSM). Figure 24(A) presents the magnetization curves at ambient conditions of samples prepared with Lubrizol U and a mixture of Lubrizol U and S_{50}-AA_{12}.The disperse phase of both samples contained Fe^{2+}/Fe^{3+} in the ratio 2:3. Magnetization curves have no specific saturation magnetization and their coercivities approach 0 Oe, which indicates the superparamagnetic properties of both samples. One of the most important observations in the magnetization curves is that the magnetization of the sample containing Lubrizol U and S_{50}-AA_{12} is significantly higher than the sample prepared with only Lubrizol U.

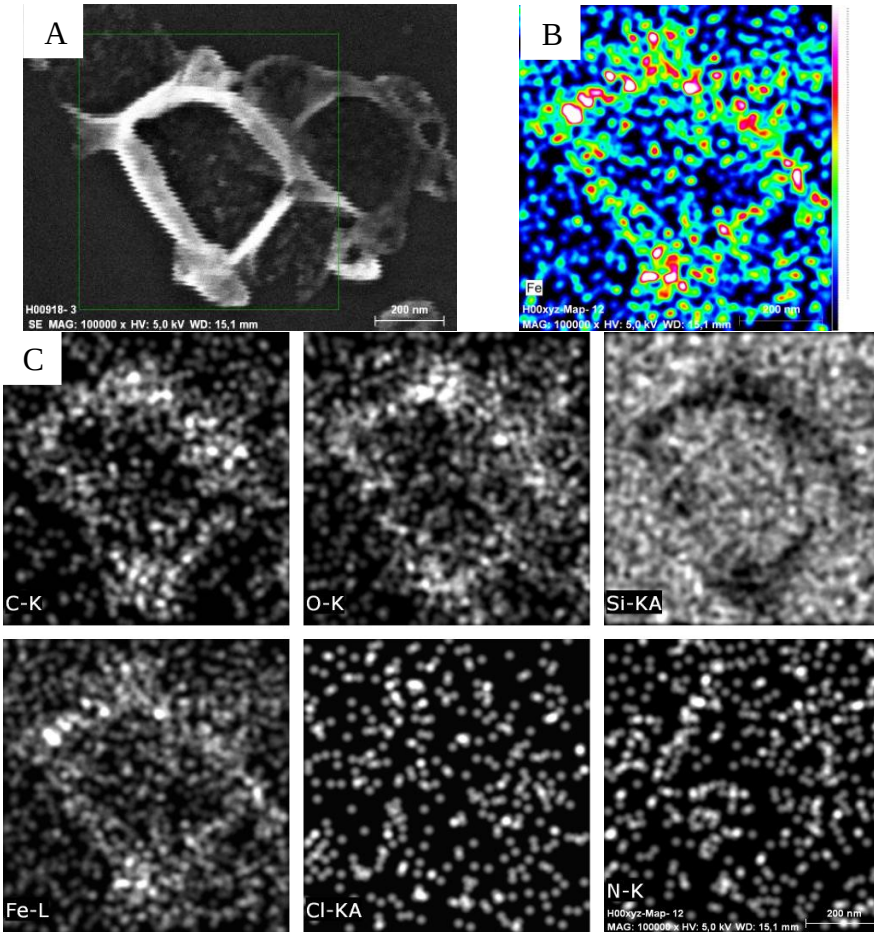

Figure 23. Elemental mapping analysis of the sample whose EDX analyses are shown in Figure 22, on a specific region shown in (A) the corresponding SEM micrograph. (B) Elemental mapping analysis of iron by coloring. (C) Elemental mapping analysis of the other elements with iron (carbon, oxygen, silicon, iron, chlorine, nitrogen, respectively).

According to the literature,[100] when an aqueous solution of Fe(III) is treated by an alkaline solution, a reddish brown precipitate of hydrated oxide is generated, which is amorphous to X-rays and corresponds probably to FeO(OH). This fact might be useful to discuss about our sample containing Lubrizol U according to its XRD pattern (black curve in Figure 21) and reddish brown color (Figure 24). The XRD pattern of the sample with Lubrizol U indicates lower crystallinity than the other sample prepared with Lubrizol U and S_{50}-AA_{12} together (red curve in Figure 21). This crystallinity difference might have an influence on the magnetic behaviors of the samples, so that more crystalline samples have better magnetic properties. How the iron oxide capsules can be magnetically separated with the help of a strong magnet is shown in the photographs of Figure 24. The sample which exhibits higher magnetization, also presents its highly magnetic behavior. This easy and efficient magnetic separation of the nanocapsules from a suspension can have promising potential application in the controlled delivery of substances under an external magnetic field.

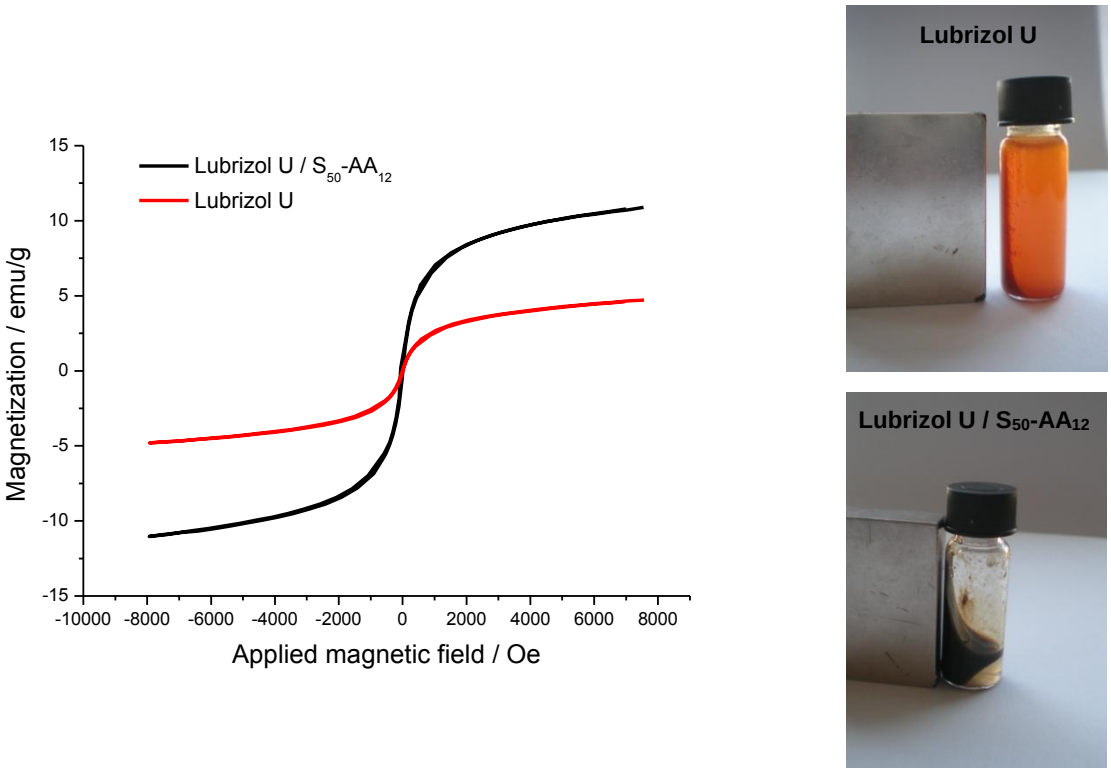

Figure 24. VSM magnetization curves of samples (A) containing only Lubrizol U (black line) and Lubrizol U/ S_{50}-AA_{12} together. (B) Photographs of the samples with only Lubrizol U and Lubrizol U/S_{50}-AA_{12} were placed next to a strong magnet.(samples SV025-08 and SV029-11of Table 9, respectively)

Effect of organic base type and amount

Electron microscopy confirmed that, as expected, no capsule or particle formation took place before the base addition, as shown in Figure 25 for a sample prepared with Lubrizol U and S_{50}-AA_{12} and Fe^{2+} as a metallic source. Few seconds after the base addition, the color of the suspension changed to black, indicating the formation of the iron oxide. The capsule shape is maintained after calcinations at 600 °C (Figure 25(C)).

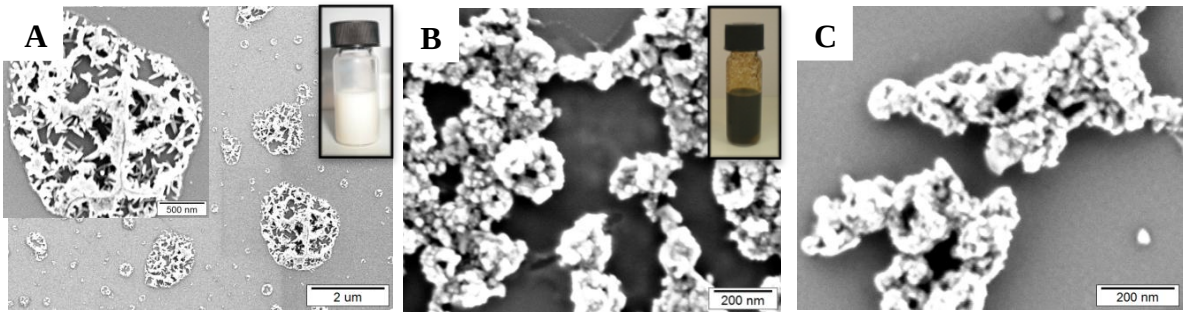

Figure 25. SEM micrographs and photographic images of a sample which contained Lubrizol U and S_{50}-AA_{12} as surfactants, (A) before Et_3N addition, (B) after Et_3N addition, and (C) after calcination. (sample SV029-01 of Table 10)

It has been reported that size, shape, and composition of iron oxide nanoparticles synthesized from aqueous Fe^{2+}/Fe^{3+} solutions by addition of a base is highly depended on the pH

value,[38, 101] which may be influenced by the type of base used. The organic base types, their variable amounts and their influences on iron oxide capsule formation in w/o systems are summarized in Table 10 .

As a comparison to Et_3N, we also investigated the ability of other organic bases to drive the crystallization iron oxides to the droplet interface: ethylenediamine, 2,2'-(ethylenedioxy)-bis-(ethylamine), 1,6-hexanediamine, and 1,4-diaminobutane. The only base that led to the formation of hollow particles was ethylenediamine, compared in Figure 26 with the results obtained with Et_3N. The completeness of the formation of the shell capsule, however, appeared to be better for the case of Et_3N.

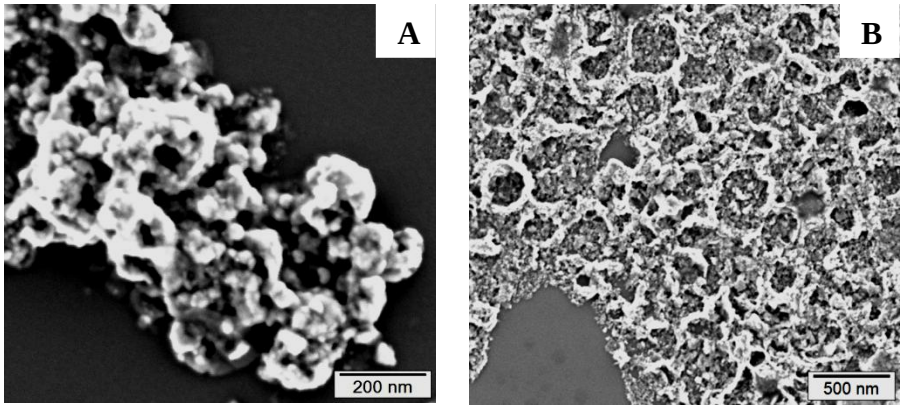

Figure 26. SEM micrographs of the samples which were prepared in presence of (A) Et_3N and (B) ethylenediamine as organic bases. (samples SV025-01 and SV026-00 of Table 10)

Samples in the presence of the S_{50}-AA_{12} block copolymer were also prepared with different types of organic bases. Et_3N, Bu_3N and ethylenediamine were added with the same metal-to-base ratio (1:3.0). SEM micrographs of these samples and the corresponding size distributions are presented in Figure 27, together with the size distributions of the particles formed. As in the case of Et_3N, the addition of Bu_3N and ethylenediamine also leads to a capsular morphology.

A difference in the size of the capsules can be observed in the histograms. The largest size of the capsules was achieved in presence of Bu_3N, while addition of ethylenediamine led to the smallest capsule size. Surface-active species between triethylammonium ions and metal hydroxide species, which tend to move to the droplet interface, may form. The size of these species should depend on the alkyl chain length of the organic base, which might be an explanation of the larger size capsules observed in presence of longer alkyl chains. TEM and electron diffraction confirmed the capsular morphology and the polycrystallinity of the sample with Bu_3N (Figure 28).

Table 10. Summary of the effects of organic base type and amount on the interfacial crystallization of iron oxides in inverse miniemulsion systems.

Sample	Precursor / surfactant	Organic base Type/Amount[(a)]	Size	SEM/TEM[(b)] (morphology)
SV025-01	Fe^{2+}/Lubrizol U	Et_3N/1:3.0	–	Capsular
SV026-00	Fe^{2+}/Lubrizol U	ethylenediamine/1:3.0	–	Capsular (poor)
SV029-00	Fe^{2+}/Lubrizol U and S_{50}-AA_{12}	Et_3N/1:1.5	–	No caps.form.
SV029-01	Fe^{2+}/Lubrizol U and S_{50}-AA_{12}	Et_3N/1:3.0	–	Capsular (poor)
SV025-10	Fe^{2+} and Fe^{3+} / Lubrizol U and S_{50}-AA_{12}	Et_3N/1:1.5	–	No caps.form
SV025-08	Fe^{2+} and Fe^{3+} / Lubrizol U and S_{50}-AA_{12}	Et_3N/1:3.0	~160	Capsular
SV029-12	Fe^{2+} and Fe^{3+} / Lubrizol U and S_{50}-AA_{12}	Bu_3N/1:3.0	~800	Capsular
SV029-13	Fe^{2+} and Fe^{3+} / Lubrizol U and S_{50}-AA_{12}	ethylenediamine/1:3.0	~120	Capsular (poor)

[(a)] Organic base amounts were indicated in terms of metal-to-base molar ratio.
[(b)] No caps.form means "no capsule formation".

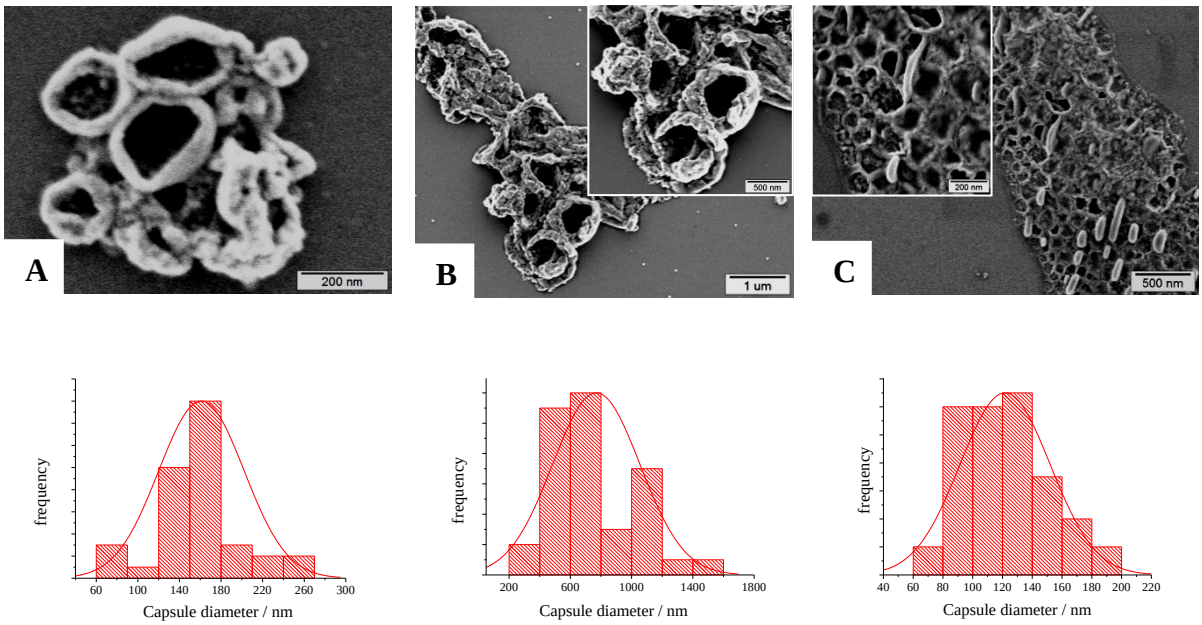

Figure 27. SEM micrographs and particle size histograms for iron oxide hollow particles prepared with (A) Et_3N, (B) Bu_3N and (C) ethylenediamine. Metal-to-base molar ratio of all the presented samples was kept constant at 1:3.0. (samples SV025-08, SV029-12 and SV029-13 of Table 10, respectively)

Finally, the effect of the base amount was investigated. Laurent et al has already mentioned that the size and shape of the nanoparticles can be optimized by adjusting pH.[102]

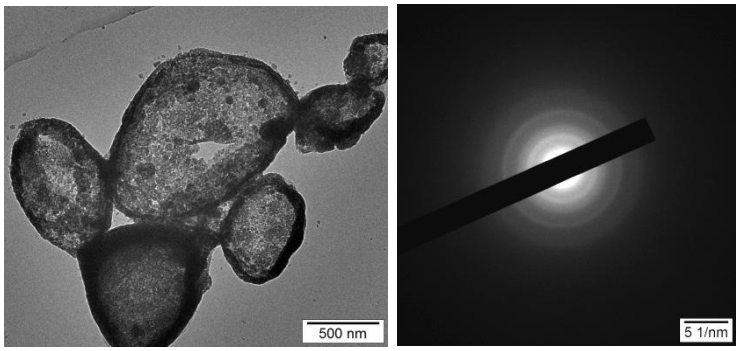

Figure 28. TEM micrograph and its corresponding diffraction pattern of sample in presence of Bu_3N as organic base. (sample SV029-12 of Table 10)

One of the difficulties of this study was to optimize the convenient base amount. The metal-to-base ratio of 1:1.5 used in previous work for zirconia and hafnia systems was further used here,[50] and compared with the double amount of base, 1:3. SEM micrographs of samples prepared at these ratios from Fe^{2+} (surfactants: Lubrizol U/S_{50}-AA_{12}) and Fe^{2+}/Fe^{3+} (surfactant: Lubrizol U) are shown in Figure 29. The results indicate that the formation of iron oxide capsules is more favorable at the higher base content.

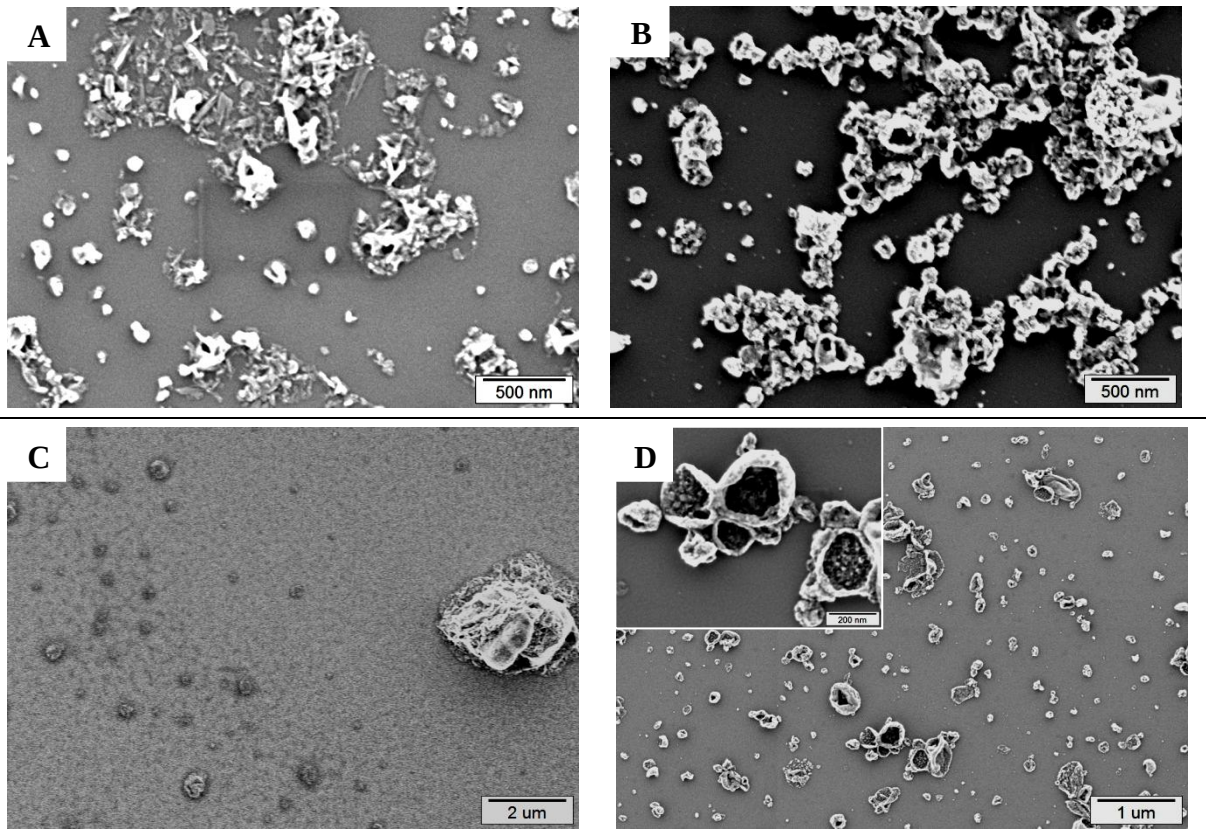

Figure 29. *First row*: SEM micrographs of samples prepared in presence of S_{50}-AA_{12} as a surfactant and Fe^{2+} with metal-to-Et_3N mol ratio of (A) 1:1.5 and (B) 1:3.0. (cf. samples SV029-00 and SV029-01 of Table 10). *Second row*: SEM micrographs of samples prepared with Lubrizol U and Fe^{2+}/Fe^{3+} at metal-to-Et_3N mol ratio of (C) 1:1.5 and (D) 1:3.0 (cf. samples SV025-10 and SV025-08 of Table 10).

Effect of the oxidation state of iron in the precursor

Iron oxide nanoparticles can be precipitated from aqueous media either by coprecipitation of Fe^{2+} and Fe^{3+}[102] or by precipitation from an Fe^{2+} solution followed by oxidation of Fe^{2+} to Fe^{3+}.[103] In this section, thus, we are going to discuss the effect of the oxidation state of iron in the precursor (i.e., the precipitation pathway) on the resulting samples. The influence of the oxidation state of iron will be first discussed for the samples containing only Lubrizol U (Table 11) and then for another group of samples prepared with Lubrizol U/S_{50}-AA_{12} (Table 12).

Samples prepared with Lubrizol U

As previous stated (cf. Figure 29(C)), samples coprecipitated from Fe^{2+}/Fe^{3+} did not show any particle/capsule formation at metal-to-Et_3N ratio of 1:1.5. Only after an increase of the amount of base (metal-to-Et_3N ratio of 1:3), hollow structures could be obtained (Figure 29(D)). However, samples prepared from only Fe^{2+} yielded capsules even at the lowest base concentration, as shown in Figure 30. The capsule formation and the crystallinity of the sample were confirmed by TEM.

Table 11. Effect of the oxidation state of iron on the interfacial crystallization of iron oxides in inverse miniemulsion systems for samples prepared in the presence of Lubrizol U as a surfactant.

Sample	Precursor	Organic base amount[(a)]	Iron oxide form	SEM/TEM[(b)] (morphology)
SV025-10	Fe^{2+}/Fe^{3+}	1:1.5	Magnetite or maghemite	No caps.form
SV025-08	Fe^{2+}/Fe^{3+}	1:3.0	Magnetite or maghemite	Capsular
SV025-00	Fe^{2+}	1:1.5	Lepidocrocite	Capsular

[(a)] Organic base of all the representatiove samples was Et_3N and the amounts were indicated in terms of metal-to-Et_3N molar ratio.
[(b)] No caps.form means “no capsule formation”.

XRD reflections of the washed sample can be assigned to lepidocrocite (γ-FeO(OH), JCPDS Card No. 44-1415), a crystal phase which was not observed in any other case. This fact indicates that different iron oxides can be achieved by changing the precursor.

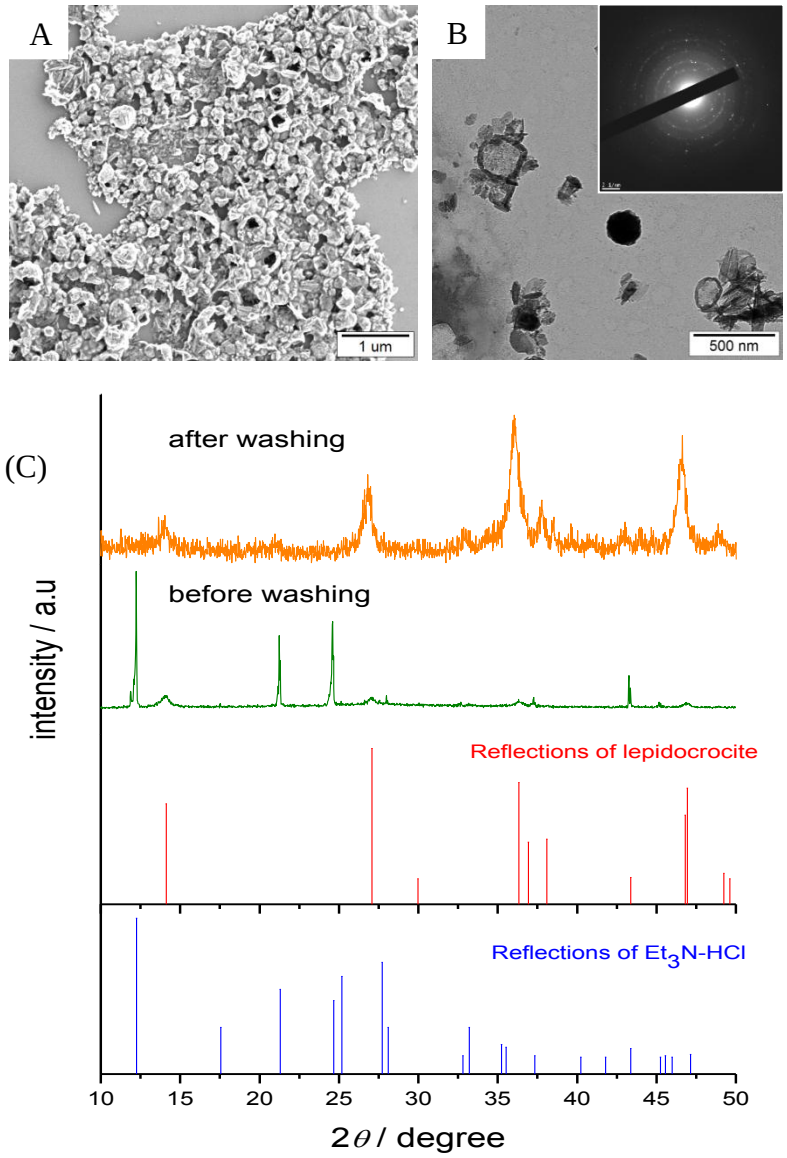

Figure 30. (A) SEM micrograph, (B) TEM micrograph and (C) X-ray diffraction pattern of the sample which contains only $FeCl_2$ as a precursor and Lubrizol U as a polymeric surfactant. (cf. sample SV025-00 of Table 3).

Samples prepared with S_{50}-AA_{12} block copolymer

Table 12. Effects of oxidation state of iron on interfacial crystallization of iron oxides in inverse miniemulsion systems for the samples in presence of Lubrizol U and S_{50}-AA_{12} as a surfactant. The samples were prepared with Et_3N as organic base and the amounts were kept constant (metal-to-Et_3N molar ratio of 1:3.0).

Sample	Precursor	Average capsule diameter	Magnetic properties[(a)]	SEM/TEM (morphology)
SV029-11	Fe^{2+}/Fe^{3+}	165	s.paramagn./lower	Capsular
SV029-04	Fe^{2+}	140	s.paramagn./higher	Capsular (poor)

[(a)] The magnetic properties column represents the magnetic behaviors of the samples and qualitative magnetization comparison of the corresponding samples to each other under the same magnetic field. s.paramagn. : superparamagnetic.

Samples prepared with S_{50}-AA_{12} copolymer and Lubrizol U by coprecipitation from Fe^{2+}/Fe^{3+} (cf. Figure 19(B)) were found to be larger in size and had a better morphology (in terms of capsule formation) than analogous samples synthesized from Fe^{2+} solutions (cf. Figure 19(C)). Better complex formation ability of the carboxylic groups of the PS-*b*-PAA with Fe^{3+} ions than Fe^{2+} ions,[100] might be a reasonable explanation of the better morphology and larger size capsules of the samples containing Fe^{2+}/Fe^{3+} as metallic precursors.

No significant differences were observed in the crystal structure and XRD patterns, presented in Figure 31, could be assigned in both cases to magnetite (JCPDS Card No. 19-0629) or, alternatively, to maghemite (JCPDS Card No. 39-1346).

In an attempt to analyze the elemental compositions of the samples whose XRD patterns have been shown in Figure 31, X-ray photoelectron spectroscopy was performed. With the help of XPS analysis, we should be able to distinguish which type iron oxide (magnetite or maghemite) were synthesized, information that could not be univocally obtained by XRD, as both phases have the same crystal structure.

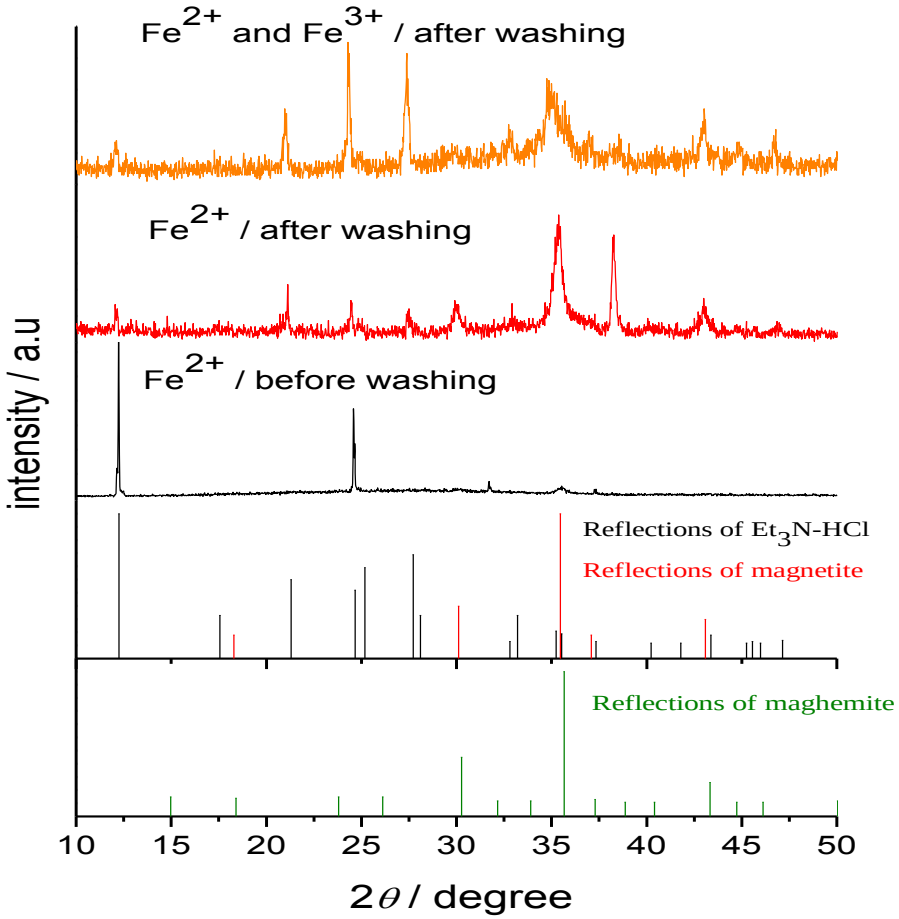

Figure 31. X-ray diffraction pattern of samples which were synthesized in presence of different metallic precursors with the reflections of magnetite, maghemite and Et_3N-HCl. (sample SV029-11 after washing, SV029-04 after washing and before washing of Table 3).

The sample containing Fe^{2+}/Fe^{3+} is mainly composed of maghemite γ-Fe_2O_3. This is confirmed by a few features of the Fe2p spectrum (Figure 32(A)). The $Fe2p_{3/2}$ peak is composed of 3 contributions, two of which are due to Fe^{3+} in maghemite, centered at 710.9 eV and a smaller contribution at 710.4 eV due to a small residual of Fe(II) (Fe(III):Fe(II)=1:0.07). Another characteristic related to the presence of Fe(III) is the presence of a satellite peak at 718.6 eV, due to *shake-up* effects (phenomenon corresponding to the emission of further photoelectron from an ion in an excited state), not found for Fe(II). The presence of Fe(II) is very limited and the form in which it is present cannot be clearly identified.

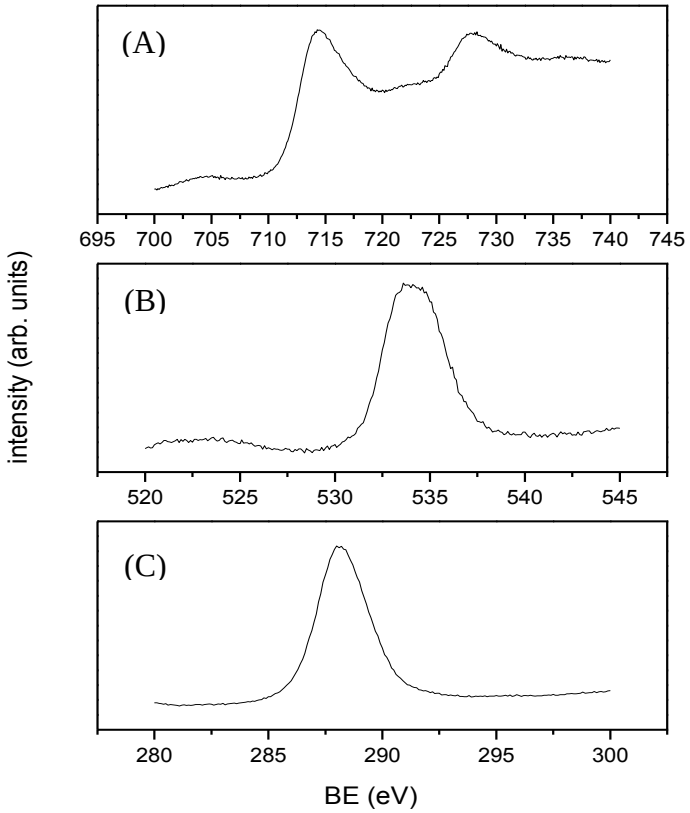

Figure 32. (A) Fe2p, (B) O1s and (C) C1s region of the sample containing Fe^{2+}/Fe^{3+} as metallic precursors.(the BE values for all the regions were not corrected for charging effects). (sample SV029-11 of Table 12)

O in hydroxyl groups, and since this contribute is important it means that the surface is highly hydroxylated, compatible with the wet synthesis approached use. This might indicate the presence of goethite (FeOOH) but it is not compatible with the shape and position of the Fe2p peak, which for the goethite is broader and centered at higher binding energies (around 711.9 eV).

The signal for O1s is very broad (Figure 32(B)), signaling the presence of different contributions. One, at 529.9 eV, is due to lattice oxygen, while the other at 531.7 eV corresponds to

Regarding the C1s peaks which is shown in the panel C of Figure 32, in both cases the main contribute is due to contamination (hydrocarbons absorbed), with further contributes due to the presence of residual surfactant, with the peaks at higher BEs corresponding to more oxidized carbons.

Table 13. Interpretation of the spectra was performed based on the article of McIntyre *et al.*[104] (values corrected for charging effects)

	Fe^{2+} / Lubrizol U and S_{50}-AA_{12}	Fe^{2+} and Fe^{3+} / Lubrizol U and S_{50}-AA_{12}	Corresponding to
C1s	284.6	284.6	C contamination
	284.8	285.0	Surfactant residual
O1s	529.8	529.9	O in Fe-O matrix
	531.4	531.7	O in hydroxyl group
Fe2p	708.1	708.4	Fe (II) residual
	710.4	710.4	Fe(III) in γ-Fe2O3
	712.5	712.7	Fe(III) in γ-Fe2O3
	719.1	718.6	Fe2O3 shake-up satellite peak

The interpretation of the other sample which prepared by Fe^{2+}/Fe^{3+} is very similar to the previous sample (see Table 13).

As shown in Table 14, both samples are contaminated. In fact, the predominant element is carbon, which originates both from hydrocarbon contamination and surfactant residuals. The sample containing Fe^{2+}/Fe^{3+} has a bigger amount of surfactant moieties since both C and N are in higher percentages with respect to the other sample. The amount of oxygen is also more than expected (for uncontaminated Fe_2O_3 the Fe:O ratio is 2:3, all other possible species have a smaller ratio, so we should have at most 1.5 times O with respect to Fe) and this can be explained in terms of surface hydroxyl groups, contaminant adsorption (some CO/CO_2 could still be present, even if most should have been removed by the UHV environment) and surfactant (there is a C=O group in Lubrizol U).

Table 14. Semi-Quantitative analysis of the samples. Values are reported in atomic %

	Fe^{2+} / Lubrizol U and S_{50}-AA_{12}	Fe^{2+} and Fe^{3+} / Lubrizol U and S_{50}-AA_{12}
C %	66.0	72.8
O %	25.6	17.3
Fe %	5.5	3.7
N %	2.9	6.2

Laurent et al. reported that the magnetic behavior of iron oxide colloids is influenced by the diameter of the crystals.[102] Higher magnetization is expected for samples with smaller capsule size. As explained previously, the capsule size of samples prepared from Fe^{2+} precursor are smaller than those coprecipitated from Fe^{2+}/Fe^{3+} (cf. Figure 20). Accordingly, the magnetization of the Fe^{2+} sample is higher, as shown in the curves of Figure 33.

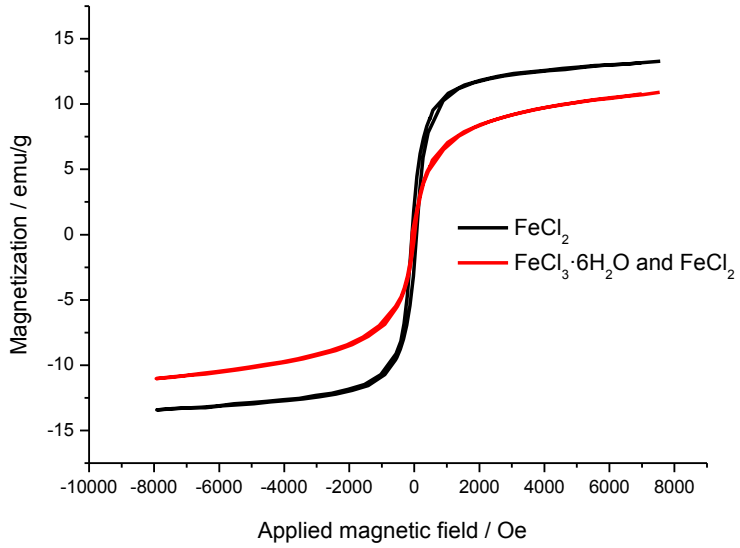

Figure 33. (A) VSM magnetization curves of the samples which contains only $FeCl_2$ and $FeCl_2$ and $FeCl_3 \cdot 6H_2O$ as metallic precursors. (sample SV029-04 and SV029-11 of Table 12, respectively).

In summary, for the magnetization curves in this section, the sample containing only Lubrizol U has lower magnetization than the samples prepared in the presence of PS-PAA. This observation was already explained in terms of the crystallinity of the samples prepared in presence of different types of polymeric surfactants. Moreover, the highest magnetization was observed for the sample with the smallest capsule size and in the presence of Lubrizol U and block copolymer.

Chapter 5

Interfacial crystallization in direct miniemulsion systems

Thinking in terms of potential biomedical applications, it would be desirable to prepare the nanocapsules in water-based systems, avoiding also the use of toxic organic amines. Therefore, we tried to achieve interfacial crystallization of iron oxides in direct miniemulsion systems using water-soluble bases.

A possibility to load metal ions at the interface of droplets is the addition of metallic salts to oil-in-water systems containing polyelectrolytic surfactants. Thus, the use of PS-*b*-PAA as a surfactant was investigated due to the ability of the carboxylic groups to bind metal cations.

Electrostatic or steric stabilization of emulsion systems to prevent coalescence can be achieved by the addition of appropriate surfactant. In the following work, we tried to find out the most convenient conditions for the stabilization of the droplets by using different types of additional surfactants, by screening the different chain length copolymers and by changing the chemistry of the hydrophobic medium.

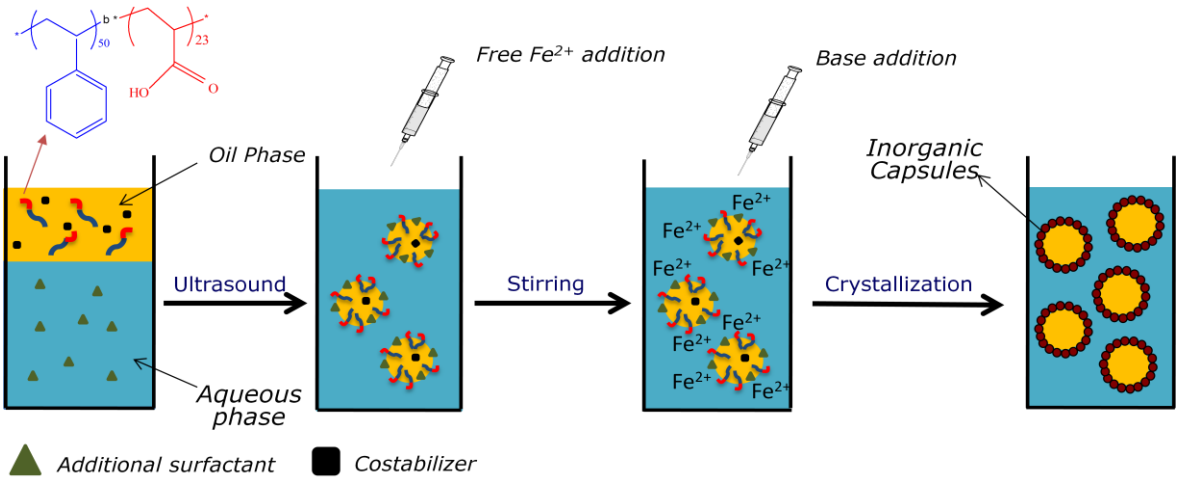

Figure 34. Schematically presentation of the direct miniemulsion systems was prepared by using PS-*b*-PAA as a surfactant.

Furthermore, some samples were also prepared by adding oleic acid in the corresponding disperse phases to stabilize the iron-oxide particles/capsules.[105]. Figure 34 depicts schematically the process followed in our o/w systems.

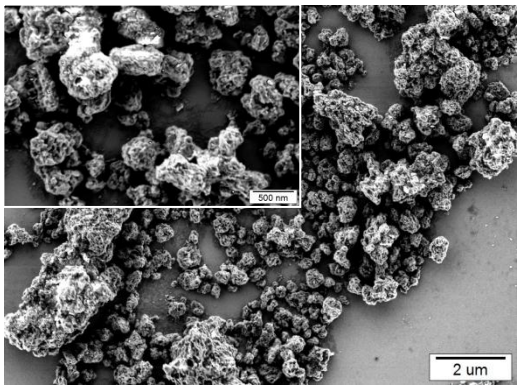

Figure 35 SEM micrographs of the sample in presence of S_{50}-AA_{30} as a surfactant.

First of all, the efficiency of the block copolymer (S_{50}-AA_{30}) as a surfactant in direct systems was investigated. The SEM micrograph shown in Figure 35 presents the emulsion reference system prepared in the absence of any additional surfactants or oleic acid. Solid particles, rather than capsules, were obtained.

Two systems were prepared to observe morphological differences due to the presence of block copolymers (S_{60}-AA_{30} and S_{50}-AA_{130}) with different chain lengths. Further stabilization of the systems were tried by adding oleic acid (22 wt% of the total iron content) to the systems.[105] Ammonia was used as a base and the amount was kept constant (metal-to-base molar ratio was kept at 1:15) along the experiments. A metal containing surface active agent, iron(II) dodecyl sulfate ($Fe(DS)_2$), was used as a metallic source and additional surfactant.

Iron(II) dodecyl sulfate ($Fe(DS)_2$, Figure 36) was synthesized by cationic exchange of sodium with iron in sodium dodecyl sulfate (SDS). The challenging part of the $Fe(DS)_2$ synthesis is the oxidation tendency of Fe^{2+} to Fe^{3+} in ambient conditions. Hence, all the synthesis and filtering processes were carried out under argon atmosphere to prevent oxidation. The characteristic properties of the synthesized $Fe(DS)_2$ were investigated by X-ray diffraction measurements. The diffractogram (Figure 36(B)) showed the most intense reflection of (001) at a 2θ value of 4.26º, which corresponds to a layer spacing of 20.7 Å. The result is comparable to the value reported by Tolbert et al. (20.6 Å).[106]

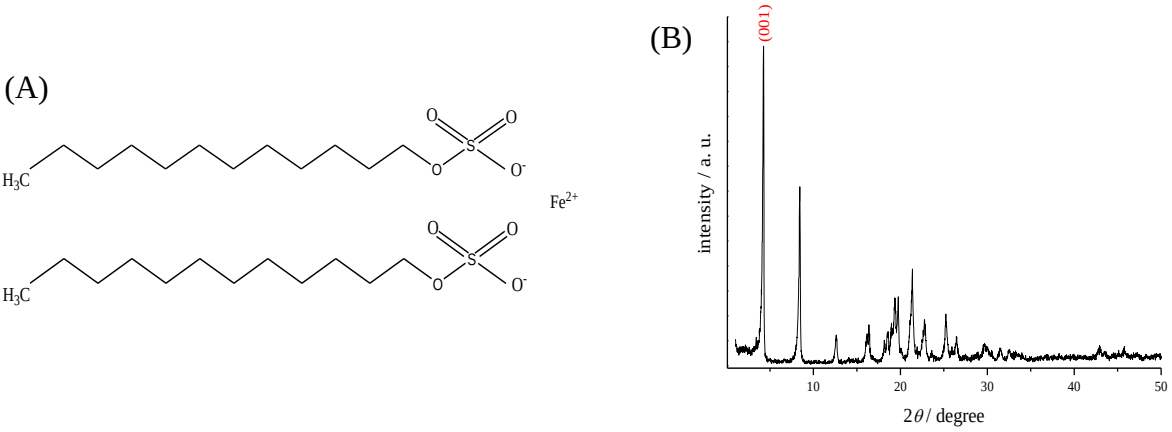

Figure 36. (A) Schematic structure of $Fe(DS)_2$ and (B) X-ray pattern of $Fe(DS)_2$.

The resulting morphologies of the systems were investigated by corresponding SEM micrographs shown in Figure 37. When the morphology of the sample prepared by using S_{60}-AA_{30} (Figure 37 (A)) is compared to the morphology of the sample by using S_{50}-AA_{130} (Figure 37 (B)), it can clearly be seen that the shorter hydrophilic part results in a better morphology. In order to bind more iron ions to the carboxylic groups of the block copolymers, a sample containing the block copolymer with longer acrylic acid part was prepared. The poorer morphology of the sample might be explained by the lower stability of the system with the block copolymer with a longer acrylic acid part.

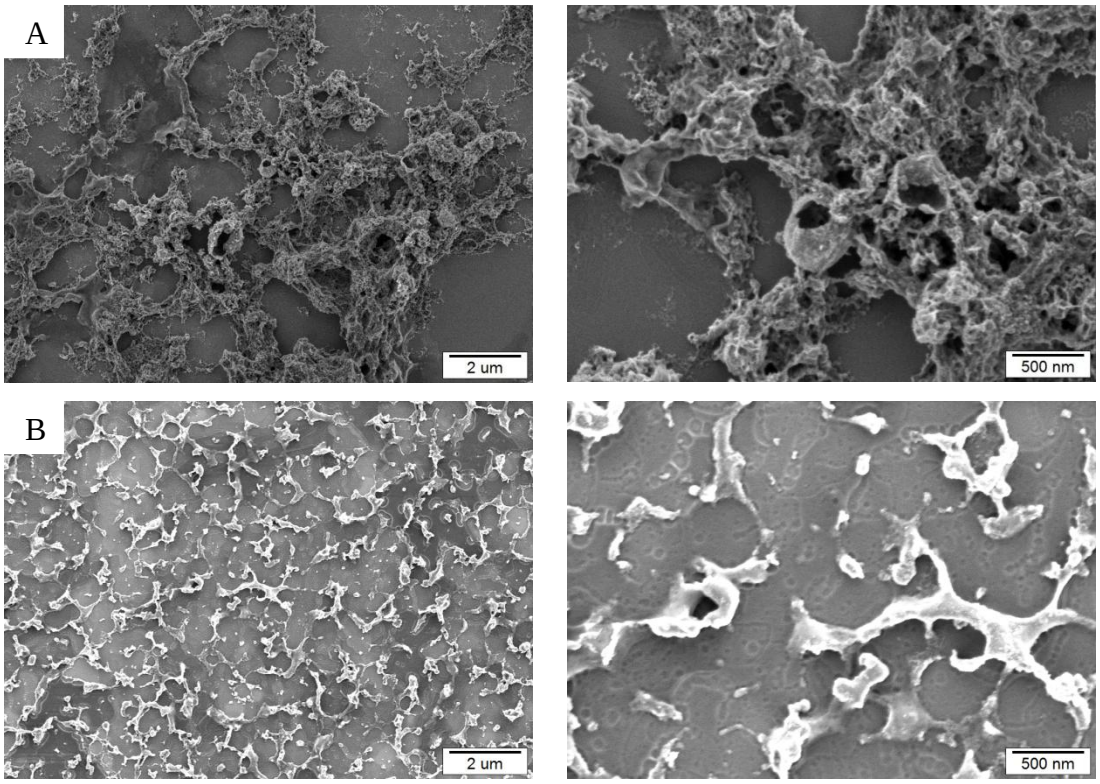

Figure 37. SEM micrographs of samples were prepared in presence of $Fe(DS)_2$ and oleic acid by using (A) S_{60}-AA_{30} and (B) S_{50}-AA_{130} as surfactants in hexadecane and the samples were treated by NH_3. (samples SV021-03 and SV027-04 of Table 4, respectively)

In an attempt to improve the results, a completely different formulation was investigated. Two further systems were prepared in the presence of S_{50}-AA_{23} and S_{50}-AA_{90}. Unlike the previous systems, SDS was used as an additional surfactant and ferrous chloride solutions were used as metallic source. Methylamine (MeA) was applied as a water-soluble base with a metal-to-base molar ratio of 1:15. As shown in Figure 38 the samples obtained with this formulation had better morphology, being especially remarkable those prepared with S_{50}-AA_{90}. This morphological improvement might be caused by the better stabilities of the systems in the second formulation.

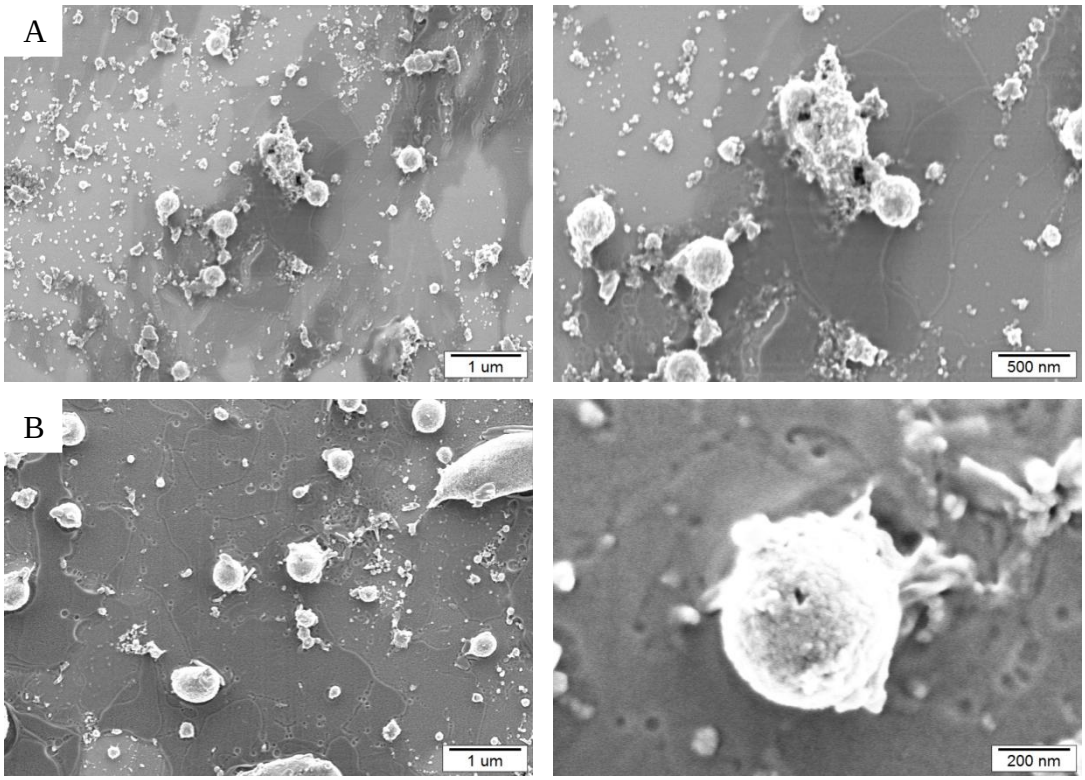

Figure 38. The samples were presented in third and fourth rows were prepared only in presence of SDS as additional surfactant by using (C) S_{50}-AA_{23} and (D) S_{50}-AA_{90} as surfactants in toluene and MeA was added as an aqueous base into both samples.(samples SV021-13 and SV021-14 of Table 4, respectively)

Finally, the effect of the costabilizer (hexadecane) was investigated. It is possible to avoid the Ostwald ripening by adding a hydrophobic agent and the stability of droplets can be improved.[107] The sample was prepared by using toluene as an oil phase with hexadecane as a costabilizer (toluene + 5 wt% hexadecane) and the morphology was compared with another sample that had only toluene as a hydrophobe.

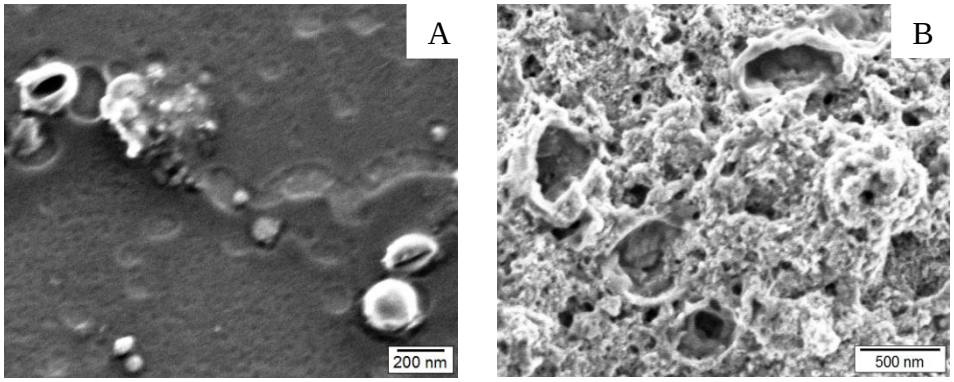

Figure 39. Micrographs of the reference samples in presence of (A) toluene and (B) toluene with 5 wt% of hexadecane as a costabilizer (cf. samples SV021-12 and SV021-07 in Table 4).

Both micrographs present capsular morphology. Nevertheless, no observable improvement was achieved in presence of the costabilizer and the elemental analysis of these capsule like structures is needed to be examined for instance by performing EDX.

In summary, it has been shown that the chain length ratio of the block copolymers is a crucial parameter for the stability of the direct miniemulsion systems. The second formulation system with S_{50}-AA_{90} resulted in the best morphology for all o/w systems. No observable improvement was detected in presence of the hexadecane as a costabilizer in toluene.

Chapter 6

Conclusions

In this work, the interfacial crystallization of cerium and various iron oxides is tried to be achieved in inverse (w/o) and direct (o/w) miniemulsion systems .

In the inverse systems, interfacial crystallization of cerium and iron oxides occurs in crystalline form at ambient conditions without any further heat treatment. Typically, samples were prepared our systems by dispersing an aqueous solution of the metallic precursors in toluene, used as continuous (oil) phase, in presence of Lubrizol U and/or PS-*b*-PAA. Organic base addition took place after ultrasonic emulsification.

For the cerium oxide system, it was shown that the presence of Lubrizol U without S_{50}-AA_{12} results in a capsular morphology. Interestingly, when the same amount of Lubrizol U with S_{50}-AA_{12} was used, solid particle rather than capsules were formed, with no remarkable changes in morphology when the amount of Lubrizol U was changed. The crystallinity of the formed ceria was confirmed by electron and X-ray diffraction for all ceria samples. The morphology of the capsules is essentially maintained after thermolytic treatment at 600 °C, after removal of the polymeric component. The presence of trimethylamine (Me_3N), triethylamine (Et_3N) and tributylamine (Bu_3N) lead to formation of capsules. The results seem to indicate that larger ceria capsules are achieved when higher amounts of base are added.

In the case of iron oxide in inverse miniemulsions, the use of a Fe(II)/Fe(III) mixture as a metallic precursor lead always to the formation of polycrystalline iron oxide capsules, and no observable morphological difference was detected due to the presence of S_{50}-*b*-AA_{12}. However, the morphology of the samples with only Fe(II) as a precursor has a strong dependence on the surfactant type: the use of Lubrizol U with S_{50}-AA_{12} resulted in hollow spheres with a poor morphology and an average size of ca. 180 nm, while with only S_{50}-AA_{12} significantly larger capsules were obtained. In general, samples coprecipitated from Fe(II) and Fe(III) yielded a better morphology than samples prepared from Fe(II). XRD patterns of the samples after washing can be ascribed to magnetite or maghemite, with the only exception of the sample prepared with Fe(II) and Lubrizol U, whose patterns correspond to lepidocrocite, γ-$FeO(OH)_2$. According to the XPS analysis, the samples containing Lubrizol U and S_{50}-AA_{12}

as polymeric surfactants either in presence of only Fe^{2+} or Fe^{2+}/Fe^{3+} were mainly composed of maghemite (γ-Fe_2O_3).Furthermore, their magnetic behaviors were also strongly depended to the surfactant type. The sample prepared with Lubrizol U and S_{50}-AA_{12} together as surfactants exhibited significantly higher magnetization than for the sample containing only Lubrizol U under the same magnetic field. Accordingly, the magnetization of the sample with smaller capsule size was relatively higher than the other sample.

Finally, we tried to conduct the interfacial crystallization of iron oxides to direct (o/w) systems. PS-*b*-PAA block copolymers were used as surfactants due to the ability of the carboxylic groups to bind metal cations. Some of the results in this case were promising, but further optimization is required. We can conclude that driving the crystallization to the interface in direct systems is more challenging than in inverse systems due to the difficulties to optimize the large variety of the synthetic parameters.

References

[1] S. Mann, *Nat. Mater.* **2009**, *8*, 781–792.
[2] X. W. Lou, L. A. Archer, Z. Yang, *Adv. Mater.* **2008**, *20*, 3987–4019.
[3] D. H., M. Buchold, C. Feldmann, *Nano Lett.* **2007**, *7*, 11.
[4] A. L. Rogach, N. Gaponik, J. M. Lupton, C. Bertoni, D. E. Gallardo, S. Dunn, N. L. Pira, M. Paderi, P. Repetto, S. G. Romanov, C. O. Dwyer, C. M. S. Torres, A. Eychmuller, *Angew. Chem., Int. Ed.* **2008**, *47*, 6538.
[5] B. J. Lemaire, P. Davidson, J. Ferre, J. P. Jamet, P. Panine, I. Dozov, J. P. Jolivet, *Phys. Rev. Lett.* **2002**, *88*, 125507.
[6] Z. W. Shan, G. Adesso, A. Cabot, M. P. Sherburne, S. A. S. Asif, O. L. Warren, D. C. Cherzan, A. M. Minor, A. P. Alivisatos, *Nat. Mater.* **2008**, *7*, 947.
[7] B. Wen, J. E. Sader, J. J. Boland, *Phys. Rev. Lett.* **2008**, *101*, 175502.
[8] W. Eerenstein, N. D. Mathur, J. F. Scott, *Nature* **2006**, *442*, 759.
[9] G. J. Snyder, E. S. Toberer, *Nat. Mater.* **2008**, *7*, 105.
[10] H. Ma, F. Y. Cheng, J. Chen, J. Z. Zhao, C. S. Li, Z. L. Tao, J. Liang, *Adv. Mater.* **2007**, *19*, 4067.
[11] O. H. Remirez, S. M. Holmes, . *J. Mater. Chem.* **2008**, *18*, 2751.
[12] D. N. Srivastava, N. Perkas, A. Gedanken, I. Felner, *J. Phys. Chem.* **2002**, *106*, 1878-1883.
[13] F. Caruso, X. Y. Shi, R. A. Caruso, A. Susha, *Adv. Mater.* **2001**, *13*, 740.
[14] Z. J. Liang, A. Susha, F. Caruso, *Chem. Mater.* **2003**, *15*, 3176.
[15] F. Caruso, M. Spasova, A. Susha, M. Giersig, R. A. Caruso, *Chem. Mater.* **2001**, *13*, 109.
[16] J. G. Castano, C. Arroyave, *ReV. Metal* **1998**, *34*, 274.
[17] S. Frank, P. C. Lauterbur, *Nature* **1993**, *363*, 334.
[18] L. X. Tifenauer, A. Tschirky, G. Kuhne, R. Y. Andres, *Magn. Reson. Imaging* **1996**, *14*, 391.
[19] K. Yamaguchi, K. Matsumoto, T. J. Fujii, *Appl. Phys.* **1990**, *67*, 4493.
[20] T. Maruyama, T. J. Kanagawa, *Electrochem. Soc* **1996**, *143*, 1675.
[21] G. A. Prinz, *Science* **1998**, *282*, 1660.
[22] L. Li, Y. Chu, Y. Liu, L. Dong, *J. Phys. Chem. C* **2007**, *111*, 2123-2127.
[23] S.-W. Cao, Y.-J. Zhu, M.-Y. Ma, L. Li, L. Zhang, *J. Phys. Chem. C* **2008**, *112*, 1851-1856.
[24] X. Y. Chen, Z. J. Zhang, X. X. Li, C. W. Shi, *Chem. Phys. Lett.* **2006**, *422*, 294.
[25] J. Kaspar, P. Fornasiero, M. Graziani, *Catal. Today* **1999**, *50* 285.
[26] Q. Fu, H. Saltsburg, M. Flytzani-Stephanopoulos, *Science* **2003**, *301* 935.
[27] G. A. Deluga, J. R. Salge, L. D. Schmidt, X. E. Verykios, *Science* **2004**, *303* 993.
[28] X. C. Zheng, X. L. Zhang, X. Y. Wang, S. R. Wang, A. S.H. Wu, *Appl. Catal. A* **2005**, *295* 142.
[29] H. Gu, M. D. Soucek, *Chem. Mater.* **2007**, *19* 1103.
[30] B. Tang, L. H. Zhuo, J. C. Ge, G. L. Wang, Z. Q. Shi, J. Y. Niu, *Chem. Commun.* **2005**, *10*, 3565.
[31] H. X. Mai, L. D. Sun, Y. W. Zhang, R. Si, W. Feng, H. P. Zhang, H. C. Liu, C. H. Yan, *J. Phys. Chem. B* **2005**, *109* 24380.
[32] Q. Wu, F. Zhang, P. Xiao, H. Tao, X. Wang, Z. H. Lu, *J. Phys. Chem. C* **2008**, *112* 17076.
[33] S. Wang, J. Zhang, J. Jiang, R. Liu, B. Zhu, M. Xu, Y. Wang, J. Cao, M. Li, Z. Yuan, S. Zhang, W. Huang, S. Wu, *Micropor. Mesopor. Mater.* **2009**, *123* 349–353.

[34] A. R. West, *Solid State Chemistry and its Applications; Wiley* **1984**.
[35] J. W. Cahn, *J. Chem. Phys.* **1965**, *42*, 93-&.
[36] J. W. Cahn, *Transactions of the Metallurgical Society of Aime* **1968**, *242*, 166.
[37] R. Muñoz-Espí, Ph.D thesis, Johannes Gutenberg-Universität **2006**.
[38] M. P. Pileni, *Nat. Mater.* **2003**, *2*, 145.
[39] M. P. Pileni, *J. Phys. Chem.* **1993**, *97*, 6961-6973.
[40] R. P. Bagwe, K. C. Khilar, *Langmuir* **2000**, *16*, 905-910.
[41] O. P. Yadav, A. Palmqvist, N. Cruise, K. Holmberg, *Colloid Surf. A-Physicochem. Eng. Aspects* **2003**, *221*, 131-134.
[42] R. Patakfalvi, I. Dekany, *Colloid Polym. Sci.* **2002**, *280*, 461-470.
[43] L. M. Qi, Y. Y. Gao, J. M. Ma, *Colloid Surf. A-Physicochem. Eng. Aspects* **1999**, *157*, 285-294.
[44] M. E. Meyre, O. Lambert, B. Desbat, C. Faure, *Nanotechnology* **2006**, *17*, 1193-1201.
[45] D. J. McClements, E. Dickinson, S. R. Dungan, J. E. Kinsella, J. G. Ma, M. J. W. Povey, *J. Colloid Interface Sci.* **1993**, *160*, 293-297.
[46] R. W. D. Montenegro, Ph.D thesis, Universität Potsdam **2003**.
[47] K. Landfester, in *Annual Review of Materials Research, Vol. 36*, **2006**, pp. 231-279.
[48] W. J. Li, X. X. Sha, W. J. Dong, Z. C. Wang, *Chem. Commun.* **2002**, 2434-2435.
[49] G. R. Bourret, R. B. Lennox, *J. Am. Chem. Soc.* **2010**, *132*, 6657.
[50] M. Hajir, P. Dolcet, V. Fischer, J. Holzinger, K. Landfester, R. Muñoz-Espí, *J. Mater. Chem.*, DOI:10.1039/C2JM15353J.
[51] R. Langer, *Nature* **1998**, *392*, 5.
[52] D. E. Bergbreiter, *Angew. Chem., Int. Ed.* **1999**, *38*, 2870.
[53] S. R. White, N. R. Sottos, P. H. Geubelle, J. S. Moore, M. R. Kessler, S. R. Sriram, E. N. Brown, S. Viswanathan, *Nature* **2001**, *409*, 794.
[54] F. Caruso, *Adv. Mater.* **2001**, *13*, 11.
[55] C. S. Peyratout, L. Dahne, *Angew. Chem., Int. Ed.* **2004**, *43*, 3762.
[56] C. S. Peyratout, H. Mohwald, L. Dahne., *Adv. Mater.* **2003**, *15*, 1722.
[57] F. Caruso, R. A. Caruso, H. Mohwald, *Science* **1998**, *282*, 1111.
[58] K. J. Pekarek, J. S. Jacob, *Nature* **1994**, *367*, 258.
[59] A. S. Utada, E. Lorenceau, D. R. Link, P. D. Kaplan, H. A. Stone, D. A. Weitz, *Science* **2005**, *308*, 537.
[60] C. I. Zoldesi, A. Imhof, *Adv. Mater.* **2005**, *17*, 924.
[61] B. M. Discher, Y. Y. Won, D. S. Ege, J. C. M. Lee, F. S. Bates, D. E. Discher, D. A. Hammer, *Science* **1999**, *284*, 1143.
[62] A. D. Dinsmore, M. F. Hsu, M. G. Nikolides, M. Marquez, A. R. Bausch, D. A. Weitz, *Science* **2002**, *298*, 1006.
[63] X. W. Lou, Y. Wang, C. Yuan, J. Y. Lee, L. A. Archer, *Adv. Mater.* **2006**, *18*, 2325.
[64] S. Y. Zeng, K. B. Tang, T. W. Li, Z. H. Liang, D. Wang, Y. K. Wang, W. W. Zhou, *J. Phys. Chem. C* **2007**, *111*, 10217.
[65] L. N. Ye, W. Guo, Y. Yang, Y. F. Du, Y. Xie, *Chem. Mater.* **2007**, *19*, 6331.
[66] C. J. Martinez, B. Hockey, C. B. Montgomery, S. Semancik, *Langmuir* **2005**, *21*, 7937.
[67] J. Liu, F. Liu, K. Gao, J. Wu, D. Xue, *J. Mater. Chem.* **2009**, *19*, 6073–6084.
[68] Y. Piao, J. Kim, H. B. Na, D. Kim, J. S. Baek, M. K. Ko, J. H. Lee, M. Shokouhimehr, T. Hyeon, *Nat. Mater.* **2008**, *7*, 242.
[69] Z. G. Feng, Y. S. Li, D. C. Niu, L. Li, W. R. Zhao, H. R. Chen, L. Li, J. H. Gao, M. L. Ruan, J. L. Shi, *Chem. Commun.* **2008**, *2629*.
[70] X. L. Yu, C. B. Cao, H. Zhu, Q. S. Li, C. L. Liu, Q. H. Gong, *Adv. Funct. Mater.* **2007**, *17*, 1397.
[71] H. L. Xu, W. Z. Wang, *Angew. Chem., Int. Ed.* **2007**, *46*, 1489.

[72] L. M. Qi, J. Li, J. M. Ma, *Adv. Mater.* **2002**, *14*, 300.
[73] X. H. Li, D. H. Zhang, J. S. Chen, *J. Am. Chem. Soc.* **2006**, *128*, 8382.
[74] H. X. Li, Z. F. Bian, J. Zhu, D. Q. Zhang, G. S. Li, Y. N. Huo, H. Li, Y. F. Lu, *J. Am. Chem. Soc.* **2007**, *129*, 8406.
[75] A. P. Alivisatos, *Science* **2000**, *289*, 736.
[76] C. Pacholski, A. Kornowski, H. Weller, *Angew. Chem., Int. Ed.* **2002**, *41*, 1188.
[77] Y. Chang, J. J. Teo, H. C. Zeng, *Langmuir* **2005**, *21*, 1074.
[78] A. Niazi, P. Poddar, A. K. Rastogi, *Current Science* **2000**, *79*, 99-109.
[79] R. S. e. al., City University of Hong Kong
[80] S. Chikazumi, S. Taketomi, M. Ukita, M. Mizukami, H. Miyajima, M. Setogawa, Y. Kurihara, *J. Magn. Magn. Mater.* **1987**, *65*, 245.
[81] A.-H. Lu, W. Schmidt, N. Matoussevitch, H. BPnnermann, B. Spliethoff, B. Tesche, E. Bill, W. Kiefer, F. SchVth, *Angew.Chem. Int. Ed.* **2004**, *43*, 4303.
[82] S. C. Tsang, V. Caps, I. Paraskevas, D. Chadwick, D. Thompsett, *Angew. Chem. Int. Ed.* **2004**, *116*, 5645.
[83] A. K. Gupta, M. Gupta, *Biomaterials* **2005**, *26*, 3995.
[84] S. Mornet, S. Vasseur, F. Grasset, P. Verveka, G. Goglio, A. Demourgues, J. Portier, E. Pollert, E. Duguet, *Prog. Solid State Chem.* **2006**, *34*, 237.
[85] Z. Li, L. Wei, M. Y. Gao, H. Lei, *Adv. Mater.* **2005**, *17*, 1001.
[86] T. Hyeon, *Chem. Commun.* **2003**, *927*.
[87] D. W. Elliott, W.-X. Zhang, *Environ. Sci. Technol.* **2001**, *35*, 4922.
[88] M. Takafuji, S. Ide, H. Ihara, Z. Xu, *Chem. Mater.* **2004**, *16*, 1977.
[89] B. Bakiz, F. Guinneton, J.-P. Dallas, S. Villain, J.-R. Gavarri, *Journal of Crystal Growth* **2008**, *310*, 3055– 3061.
[90] E.-M. Rosenbauer, K. Landfester, A. Musyanovych, *Langmuir* **2009**, *25*, 12084-12091.
[91] N. Nabih, R. Schiller, I. Lieberwirth, E. Kockrick, R. Frind, S. Kaskel, C. K. Weiss, K. Landfester, *Nanotechnology* **2011**, *22*.
[92] H. Y. Wen, G. Gao, Z. R. Han, F. Q. Liu, *Polymer International* **2008**, *57*, 584-591.
[93] I. K. a. E. Erkizia, *Phys. Status Solidi* **2010**, *C 7*, 2697–2700.
[94] A. K. Gupta, S. Wells, *IEEE Trans. Nanobiosci.* **2004**, *3*, 66.
[95] Y. Deng, L. Wang, W. Yang, S. Fu, A. J. Elaissari, *Magn. Magn. Mater.* **2003**, *257*, 69.
[96] C. T. Seip, E. E. Carpenter, C. J. O'Connor, V. T. John, S. C. Li, *IEEE Trans. Magn.* **1998**, *34*, 1111.
[97] J. R. Vidal-Vidal, J.; Lopez-Quintela, M. A., *Colloids Surf.* **2006**, *288*, 44.
[98] Z. Y. Jia, W.; Yangcheng, L.; Jingyu, M.; Guangsheng, L, *React. Funct. Polym* **2006**, *66*, 1552.
[99] L.-P. Zhu, H.-M. Xiao, W.-D. Zhang, G. Yang, S.-Y. Fu, *Cryst. Growth Des.* **2008**, *8* 957–963.
[100] N. N. Greenwood, A. Earnshaw, *Chemistry of the elements*, **1997**.
[101] A.-H. Lu, E. L. Salabas, F. Schueth, *Angew. Chem.-Int. Ed.* **2007**, *46*, 1222-1244.
[102] S. Laurent, D. Forge, M. Port, A. Roch, C. Robic, L. V. Elst, R. N. Muller, *Chem. Rev.* **2008**, *108*, 2064-2110.
[103] A. Mantion, F. Gozzo, B. Schmitt, W. B. Stern, Y. Gerber, A. Y. Robin, K. M. Fromm, M. Painsi, A. Taubert, *J. Phys. Chem. C* **2008**, *112*, 12104-12110.
[104] N. S. McIntyre, D. G. Zetaruk, *Anal. Chem.* **1977**, *49*, 11.
[105] K. Landfester, L. P. Ramirez, *J. Phys.-Condensed Matter.* **2003**, *15*, S1345-S1361.
[106] S. H. Tolbert, P. Sieger, G. D. Stucky, S. M. J. Aubin, C.-C. Wu, David N. Hendrickson, *J. Am. Chem. Soc.* **1997**, *119*, 8652-8661.

[107] R. Muñoz-Espí, Y. Qi, I. Lieberwirth, C. M. Gómez, G. Wegner, *Chem.—Eur. J.* **2006**, *12*, 118-129.

Acknowledgement

It would not have been possible to write this master thesis without the help and guidance of the kind people around me, to only some of whom it is possible to express my gratitude here.

Above all, I would like to thank Professor Katharina Landfester for giving me the opportunity to be a part of her group on such an interesting research topic and in such nice working conditions. Besides, I will always respect to her knowledge and ability to follow, orient and carry every single project one step further in her group.

I would also like to thank, my second referee PD Dr. Ulrich Ziener, who kindly agreed to be my second referee for this thesis. Furthermore, it was a big honor for me to be introduced to Max Planck Institute for Polymer research by him.

I owe very special thanks to my project leader and "*the best teacher in my life*", Rafael Muñoz-Espí for his "*first*" endless patience, guidance and understanding. I will never forget any single second when he was teaching me the basics of miniemulsions, inorganics and chemistry as well as the scientific writing skills. I wish him the very best in the rest of his life.

In the TEM sections I have been aided for many times in running the equipment by Ingo Lieberwirth, I appreciate him because of his useful comments and suggestions. I would like to thank especially to Gunnar Glaßer for tutor me SEM and for his effort to analyzing my samples with EDX. I owe very special thanks to Silvia Gross and Paolo Dolcet because of their assistance for XPS measurements and their kindly helps for the data analysis. Barat Khurbanjan is thanked for his guidance in the measurements of VSM even if he was in hurry because of his PhD thesis. I am also very thankful to *Michael Steiert* for the XRD measurements.

A very special thanks is addressed to Daniel Crespy, who was a great friend and a very helpful teacher as well. It will be a great honor for me to play in the same team on the next MPIP football championship.

I am thankful to all my lecturers from Ulm University for their devotion and labour. Particularly, I owe my deepest gratitude to, Professor Paul Ziemann, Professor Ulrich Herr and Anna Musyanovych for motivating me to learn more about materials and polymer science. It also gives me great pleasure in acknowledging my Professors Ersan Kalafatoglu, Recep Artir and Seval Genc from Material and Metallurgical Engineering Department in Marmara University, I will never forget their valuable classes. Particularly, if my Professor Ersan Kalafatoglu had not encouraged me, I would not have been in Germany for my master degree.

I owe my gratitude to Nesrin Horzum Polat for her big help in many part of my life especially writing process of this thesis. It was a really great enjoy to be a neighbor in the office with her. I would also like to thank Margherita Mari, her "*sisterly*" and lovely behavior will be all the time remembered by her brother. Moreover, I am indebted to my colleagues Rengin Pekoz, Hélène Freichels, Jian Chen, Gerard Sánchez Reina, Matthew A. Hood, Viktor Fischer, Umaporn Paiphansiri, Bora Inci and all the members of "*Lokomotive Landfester*" football team for their helps and great company. It was a pleasure for me to know them and spend this thesis time with them.

I owe very special thanks to Mehmet Can Yagci and Tuna Öztürk to being my brothers, my "*fellow travelers*". Your presence in my life will always encourage me to carry on even if we are away from each other.

I would like to thank a lot to my aunt and her lovely family. They have been supporting me since the very first time in Germany and giving me a chance to feel like a member of their great family.

Most importantly, none of this would have been possible without the love and patience of my lovely parents, Fikret Varol and Sema Varol and especially, my sister, "*the half of my life*", Bilge Varol. I owe them the deepest gratitude.